Impact of mesoscale eddy parameterization on Arctic Atlantic Water circulation and heat transport in the eddy-permitting grey zone

Per Pemberton[1], Iréne Wåhlström[1], and Sam Fredriksson[1]

[1]Swedish Meteorological and Hydrological Institute Göteborgseskadernas plats 3, S-426 71 Västra Frölunda, Sweden.

Correspondence: Per Pemberton (per.pemberton@smhi.se)

Abstract. The Arctic Ocean is undergoing rapid change, yet many CMIP-type climate models struggle to accurately represent its circulation and water masses. A key feature of the system is the topographically controlled boundary currents that transport warm, saline Atlantic Water northward at intermediate depths into the Atlantic Water layer. An important process affecting these boundary currents is the lateral flux of heat and salt driven by mesoscale eddies. Because the deformation radius is rel-
5   atively small in the Arctic Ocean, numerical simulations require kilometer-scale resolution to fully capture eddy dynamics. Most of the current climate models, however, operate in a non-eddying regime, relying on mesoscale eddy parameterizations – typically combining isopycnal diffusion (Redi) with eddy-induced advection (Gent & McWilliams, GM). As horizontal resolution increases, future models will shift from an eddy-parameterized to eddy-permitting regime, entering a grey zone where eddies are only partially resolved and the role of GM parameterization becomes less straightforward. This study investigates
10 the use of GM parameterization in eddy-permitting models, focusing on its effect on the northward transport of Atlantic Water in the Nordic Seas and Arctic Ocean. We conduct realistic simulations where we vary GM diffusivity strength and test two different GM scalings. These experiments are compared with a high-resolution model-truth simulation and observational data. Consistent with earlier idealistic studies, we find that omitting the GM parameterization excludes important eddy–mean flow interactions, which in our case results in stronger meridional overturning, barotropic circulation, and northward transport. Con-
15 versely, applying GM results in weaker circulation and dampens resolved eddy fluxes, while the parameterized fluxes introduce biases, particularly in the temperature distribution in the Greenland Sea.

1   Introduction

In the Arctic region the effects of antropogenic global warming are most pronounced, with regional warming reaching up to four times the global average (Rantanen et al., 2022). The region is dominated by the Arctic Ocean, a nearly landlocked body
20 of water that remains largely ice-covered year-round. The effects of ongoing global warming are reshaping the Arctic Ocean where key changes include the significant reduction in summer sea-ice extent (Stroeve and Notz, 2018) and the Atlantification of the Atlantic sector of the Arctic Ocean where a warming of the Atlantic Water (AW) inflow drives the region to a more Atlantic-like state (Lind et al., 2018; Polyakov et al., 2020, 2023). These transformations are expected to trigger cascading

impacts on the ecosystem, including increased ocean acidification and the loss of critical habitats (AMAP, 2018, 2025; Barton
25 et al., 2018).

Globally the Arctic Ocean connects the Pacific Ocean and North Atlantic Ocean through a number of key gateways (see Figure 1). It receives warm and salty water from the Atlantic Ocean and warm and less salty water from the Pacific Ocean (Østerhus et al., 2019). Through air–sea heat loss, input of freshwater from rivers and precipitation, and sea ice melt and formation it transforms the inflowing waters to less salty and colder water masses that are then exported back to the North
30 Atlantic Ocean and thus impact the global ocean circulation (Timmermans and Marshall, 2020; Rudels and Carmack, 2022). The AW circulation plays a crucial role in shaping the Arctic Ocean water masses. Due to relatively weak gradients in density and planetary vorticity the northward flow of AW across the Nordic Seas and Arctic Ocean is to a large degree contained in topographically steered boundary currents circulating cyclonically around the basins (Nøst and Isachsen, 2003). After crossing the Greenland–Scotland Ridge (GSR) the flow splits up in two branches, the Norwegian Atlantic Slope Current and the Nor-
35 wegian Atlantic Frontal Current, see Figure 1. In the eastern Nordic Seas the boundary currents loses heat to the atmosphere and central parts of the basins (Bosse et al., 2018) as it flows poleward. Then in the northern parts of the Nordic Seas it splits up in two poleward branches and one southward recirculating branch (Fig. 1).

Once the AW reach the Arctic Ocean the upper water mass is strongly cooled and freshen forming the Polar Surface Water (PSW), while the intermediate layer remains relatively warm and forms the AW layer. Out of the two poleward branches the
40 Barents Sea branch experiences a strong cooling through air–sea exchange, whereas the Fram Strait branch retains more heat, making it the primary source of oceanic heat for the AW layer (Rudels et al., 2011). In the central parts of the Arctic Ocean the main AW layer flow continues to follow the topographic slope around the deep basins before it eventually exits through the Fram Strait (Aksenov et al., 2011; Rudels et al., 2011). In the central Arctic Ocean the cold halocline strongly inhibits upwards heat transport from the AW layer to the PSW although recent observations show a weakening of the halocline and increased
45 heat flux in the Eurasian basin (Polyakov et al., 2020). Occasionally AW is seen to upwell to the shelf regions potentially impacting sea ice melt and marine productivity (Dmitrenko et al., 2010; Li et al., 2022). The AW is also seen to flow into the fjords of northern Greenland and potential melting the ice tongues flowing out of the Greenland Ice Sheet (Jakobsson et al., 2020; Wekerle et al., 2024).

To understand the drivers and consequences of a warming Arctic Ocean numerical models are invaluable tools, especially
50 since the prevailing sea-ice conditions make it difficult to sample the ocean both in-situ and remotely. However, the Arctic Ocean and particularly the intermediate AW layer have proved difficult to model accurately. Early Arctic model intercomparison projects identified an overly thick and cold AW layer in most models (Holloway et al., 2007; Karcher et al., 2007), and recent studies show that the problems still remain. Particularly the oceanic components of the coupled models participating in the last two iterations of the Climate Model Inter Comparison Project (CMIP5 and CMIP6) have a poor representation of
55 the Arctic water masses and a large intramodel spread (e.g. Khosravi et al., 2022; Shu et al., 2019, 2023; Heuzé et al., 2023). The majority of the participating models in CMIP6 have a resolution of about 1° in the ocean which means that small scale processes like mesoscale eddies needs to be parameterized (Fox-Kemper et al., 2019), and although the resolution in these
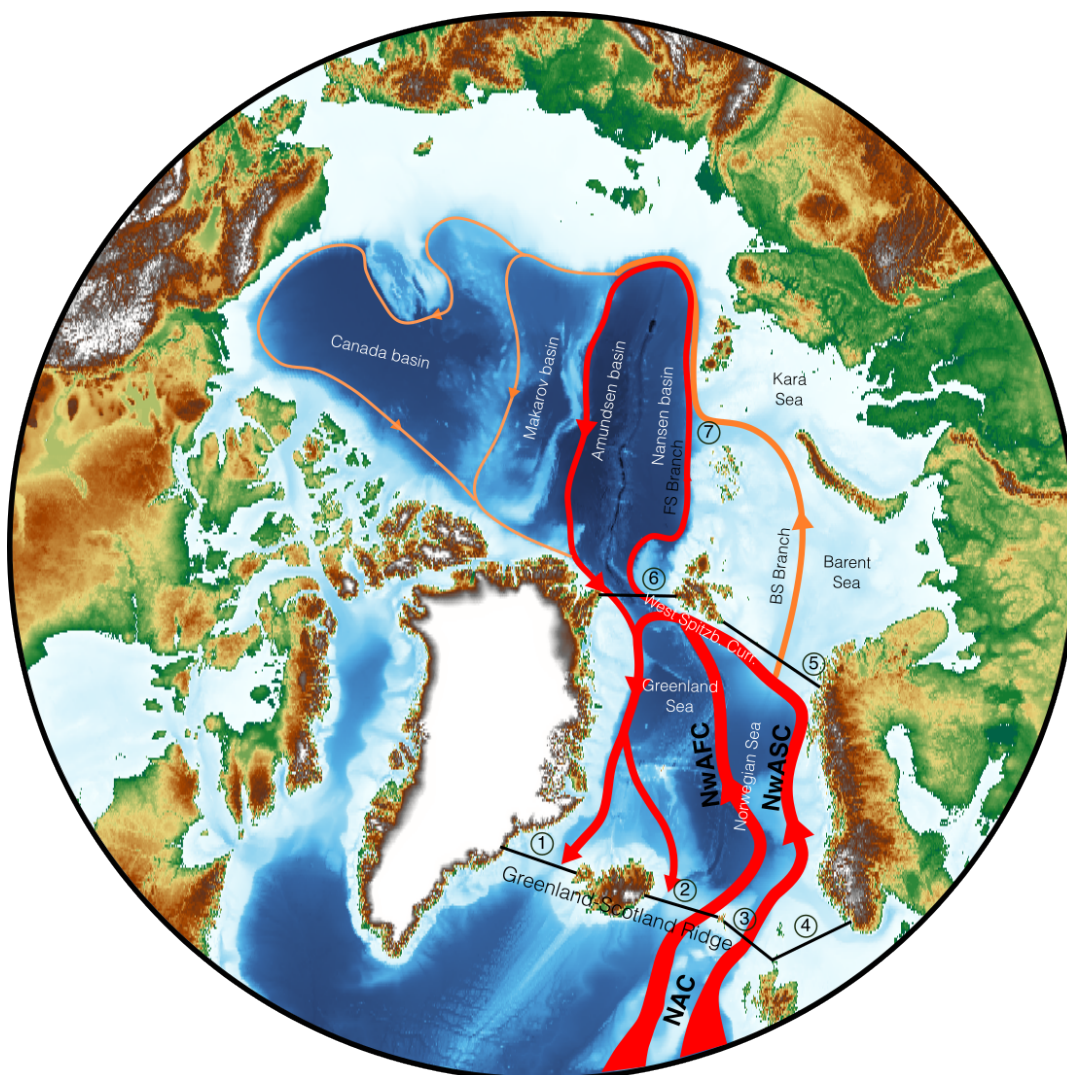
Figure 1. A schematic of the Atlantic Water circulation across the Nordic Seas and Arctic Ocean also including names of places mentioned in the text. Within the Nordic Seas the North Atlantic Current (NAC) is split up in two northward flowing branches: Norwegian Atlantic Slope Current (NwASC) and Norwegian Atlantic Frontal Current (NwAFC). Then in the northern end two different branches enter the Arctic Ocean: the warmer Fram Strait (FS) branch and the colder Barents Sea (BS) branch. The figure also shows the gateways (black lines) used for computing transports. They are numbered according to 1=Denmark Strait, 2=Iceland–Faroe, 3=Faroe–Scotland, 4=Scotland–Norway, 5= Barents Sea Opening, 6=Fram Strait, and 7=St. Anna Trough.

models is slowly increasing we are not expected to have fully mesoscale resolving models within the next ten years (Hewitt et al., 2022).

60   Oceanic mesoscale eddies play a key role in the large-scale ocean and climate system (e.g. Hewitt et al., 2022), and give sizeable contributions to the total global scale transport of heat and salt (Dong et al., 2014). Mesoscale eddies have gained more attration in the Arctic Ocean as well, since they are believed to be important for the large-scale circulation and heat transport (Timmermans and Marshall, 2020; von Appen et al., 2022; Li et al., 2024). As AW flows north across the Nordic Seas, mesoscale eddies are seen to redistribute heat and salt between the boundary current and deeper interior (Isachsen et al.,

65   2012). Similar processes are seen inside the Arctic Ocean as well, where in addition to the lateral transport eddy fluxes also impact the vertical heat flux (Pnyushkov et al., 2018). Here sea ice has an important role in that it contributes to dissipation of near-surface eddies seasonally, while below the strong halocline subsurface eddies can be formed in the interior of the Arctic Ocean (Meneghello et al., 2021).

The dominant spatial scales of baroclinic ocean mesoscale eddies can broadly be characterized by the first baroclinic de-

70   formation radius (Hallberg, 2013). At high latitudes, the deformation radius is relatively small, typically below 15 km, see Figure 2a. This has implication for modelling of the AW circulation as model resolution needs to be at kilometer-scale to be in a fully eddying regime (e.g. Wekerle et al., 2017; Li et al., 2024). If the interactions between the eddies and energetic boundary current are missing this will lead to biases in the mean flow and northward heat transport. In coarse resolution ocean models (like the ones used in CMIP6) the choice to parameterize mesoscale eddy effects is straightforward since there is a

75   clear separation between the resolved large scale dynamics and the unresolved mesoscale dynamics (since $\mathbf{u}'$ is essentially zero in Eq. 1 below). The most common parameterization for mesoscale eddy tracer transport in current non-eddying ocean models combines a rotated isopycnal diffusion (Redi, 1982) with an eddy-induced advection (Gent and McWilliams, 1990, hereafter GM). The Redi scheme leads to a downgradient flux and reduction of tracer variance, while GM scheme tends to flatten isopycnals via an eddy-induced transport up the density gradients.

80   In the next generation of climate models used in e.g. CMIP7 many ocean models can be expected to increase resolution up to 1/4° (e.g. Hewitt et al., 2022), and will instead operate in an eddy-permitting regime in the Nordics Seas and Arctic Ocean. In the eddy-permitting regime the use of the GM scheme becomes less straightforward as it might have a negative impact on the resolved dynamics (Hallberg, 2013; Mak et al., 2023). Following Ruan et al. (2024) we can formulate the underlying problem using a Reynolds decomposition of the velocity (specifically the tracer advective velocity) as

$$\mathbf{u} = \overline{\mathbf{u}} + \mathbf{u}' + \mathbf{u}^*, \qquad \overline{\mathbf{u}'} = 0, \tag{1}$$

85   where overbar denotes Reynolds (time) average, $\mathbf{u}'$ the resolved eddies and $\mathbf{u}^*$ parameterized eddies. The GM scheme specifies

$$\mathbf{u}^* = \nabla \times (\mathbf{e_z} \times \kappa_{GM}\mathbf{s}), \qquad \mathbf{s} = \frac{\nabla_H \rho}{-\partial \rho/\partial z}, \tag{2}$$

where ρ is the density, $\mathbf{s}$ the isopycnals slopes in the horizontal directions, $\mathbf{e_z}$ the vertical unit vector, and κ_{GM} the GM diffusivity coefficients. If the eddy-permitting models omit the GM scheme the full eddy-mean flow interactions will not be

EGUsphere
Preprint repository
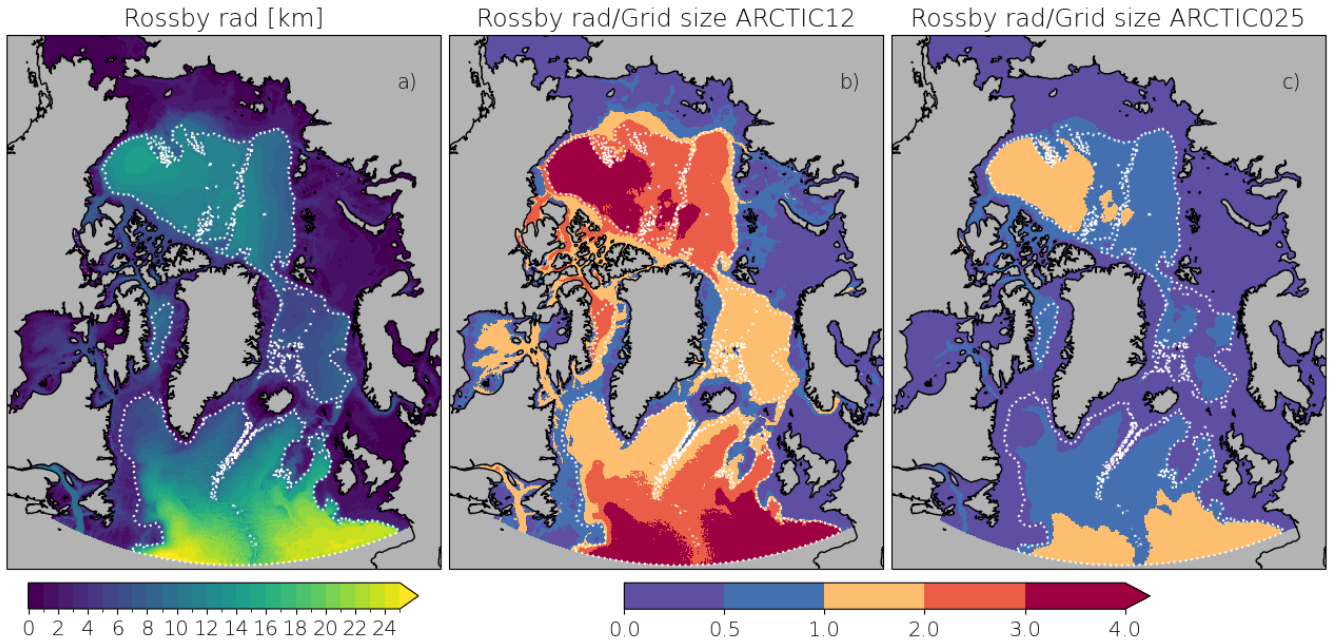
Figure 2. The first baroclinic deformation (Rossby) radius L_d [km] computed from ARCTIC12 (left), the ratio of $L_d/min(dx, dy)$ for ARCTIC12 (middle) and ARCTIC025 (right). At a ratio greater than 1.0 the model configurations has at least two grid points per L_d and starts to resolve most of the eddy field. All fields are averaged over the period 1979–2017. The white dotted line shows the 1500 m depth contour.

accounted for by $\mathbf{u}'$ (since it does not resolve all mesoscale eddies). On the other hand, if the GM scheme is used the resolved

90   eddy field ($\mathbf{u}'$) will be strongly dampened by the flattening effect $\mathbf{u}^*$ has on isopycnals (Mak et al., 2023).

For global or large-scale models where the deformation varies across the computational domain the models capability to resolve eddies will vary and there is a numerical grey zone whether to use the GM parameterization or not. There is a field of ongoing research to handle the negative impact of the GM scheme and make it scale-aware. Several different approaches have been proposed, e.g., using a resolution function based on deformation radius (Hallberg, 2013), coupling energy backscatter to

95   GM via negative viscosity (Bachman, 2019; Jansen et al., 2019), or filtering out the small scale field before GM is applied (Mak et al., 2023). However, these methods are far from standard practice in ocean modelling and not readily available in global climate models. Understanding what effect the use of the "standard" GM scheme has on the ocean circulation and heat transport in realistic ocean simulations, and different parts of the model domain, is therefore important since it might limit the next generation of climate simulations.

100   In this paper we evaluate the effect of resolved and parameterized mesoscale eddy fluxes on the AW circulation in the Nordic Seas and Arctic Ocean, where we primarily study the AW layer at intermediate depths. We use two realistic pan-Arctic Ocean NEMO4-SI³ configurations, one intermediate resolution (1/4°) configuration that is eddy-permitting and one high resolution (1/12°) configuration that serves as a model truth. The regional grids are extracted from preexisting global

grids, and most of our settings follow what is used in global models. We focus on the intermediate resolution configuration that

105   is in a grey zone whether the GM parameterization should be used or not. Through a set of experiments we assess the impact of the GM scheme by varying the strength of the GM diffusivity coefficient in the intermediate resolution configuration and then compare the results to the high resolution configuration, that is more eddy active and explicitly resolves most of the eddy fluxes, as well as to observational estimates. We diagnose the partitioning of the total kinetic energy, barotropic and overturning circulation, transports across key gateways, temperature in the AW layer as well as the change in hydrographic structure along

110   the northward AW pathway in the Nordic Seas and Arctic Ocean. The paper is structured as follows: in section 2 we present the model configurations, experiment setup, bservational data, and evaluation metrics, this is followed by the results in section 3, and then we end with a summary and conclusions.

2   Methods and data

2.1   The NEMO–SI3 Arctic Ocean configurations

115   In our study we use two NEMO4.0.4-based regional Arctic configurations covering the same geographical region and differing only in their horizontal resolution. The configurations are constructed by extracting sub-domains of already existing global configurations from the ORCA family of grids. Here we base our regional configurations on the global ORCA12 and ORCA025 grids, nominal resolutions of $1/12°$ and $1/4°$, and call them ARCTIC12 and ARCTIC025, respectively. The regional domain covers the Arctic Ocean including the Nordic Seas and has two open boundaries towards the Bering Sea and North Atlantic

120   Ocean.

The ORCA grids have a refinement of the grid size polewards and in our regional domains the horizontal resolution of ARCTIC12 (ARCTIC025) varies between 2–7 (3–20) km with domain mean resolutions of 5 (14) kms. The first baroclinic Rossby radius is of O(1–15 km) in the Arctic Ocean and the Nordic Seas (see Fig 2), which leaves ARCTIC12 in an eddy-permitting to eddy-resolving regime, and ARCTIC025 in a eddy-permitting regime. The vertical coordinate is discretised using

125   the z* formulation with 66 layers ranging from 5 m in the surface to 152 m at depth.

Momentum advection uses the vector-invariant formulation together with the energy and enstrophy conserving scheme, and tracer advection the Flux Corrected Transport (FCT) scheme of 4th order in both the horizontal and vertical directions. The lateral momentum diffusion uses a bi-laplacian operator applied in the horizontal directions together with a viscosity coefficient that is scaled by a defined velocity scale $U_{visc} = 0.185$ and the horizontal model grid scale L. The lateral tracer diffusion uses

130   a laplacian operator applied in the isopycnal directions (Redi scheme) together with a diffusivity coefficient that is scaled by a defined velocity scale $U_{diff} = 0.0193$ and L.

For the eddy-induced advection (GM scheme) we use two different formulations for the GM diffusivity coefficient κ_{GM}. For two of the experiments we use a standard scaling $\kappa_{GM} = \frac{L_d^2}{T}$ based on Treguier et al. (1997) where T is the inverse baroclinic timescale and L_d the Rossby radius. For one experiment we instead use the new scaling $\kappa_{GM} = \alpha E \frac{N}{M^2}$ based on

135   the GEOMETRIC scheme (Mak et al., 2018) where N is the buoyancy frequency, M^2 the magnitude of the lateral buoyancy gradient, E the total eddy energy, and α is the eddy efficiency parameter. The GEOMETRIC scheme solves a prognostic

equation for E. The α parameter and the dissipation timescale (λ) need to be tuned to the specific application (see Mak et al., 2018), we use $\alpha = 0.045$ and $\lambda = 100$ days.

The vertical diffusivity and viscosity are computed by a turbulent closure scheme based on the prognostic equations for the

140 turbulent kinetic energy and its dissipation rate (TKE scheme). The background values for vertical diffusivity and viscosity are tuned down to $5.4 \cdot 10^{-6}$ and $5.4 \cdot 10^{-7}$ m^{2}s^{-1}, respectively, due to the low mixing nature of the Arctic Ocean (Zhang and Steele, 2007). Both the surface and bottom stresses are solved implicitly, and use a non-linear formulation with a drag coefficient of $1.0 \cdot 10^{-3}$.

Open lateral boundary conditions for sea surface height (SSH) and barotropic velocities use the Flather radiation scheme,

145 3-dimensional baroclinic velocities and tracers use the Orlanski radiation scheme. Close to the open boundaries we define a buffer layer consisting of 8 (4) rim points for the ARCTIC12 (ARCTIC025) configuration. The total volume flux across the boundaries is balanced offline to avoid a drift in total ocean volume. At the moment no tidal components are included.

The sea ice model discretises the ice thickness distribution using ten ice categories with an expected domain average ice thickness of 2 meter. Five vertical ice layers are used for the enthalpy (temperature and salinity profile) computations. Sea

150 ice advection uses the flux corrected 5th order Ultimate-Macho scheme, and a landfast ice parameterization is utilized. Snow conductivity is reduced to 0.24 W(mK)$^{-1}$ following tuning tests of total sea ice volume and thickness in the Arctic Ocean.

2.2 Experiments

To understand how horizontal resolution and parameterized eddy fluxes impact the AW circulation we run a set of five experiments. In one experiment we run the high resolution configuration ARCTIC12 without GM scheme and this serves as a model

155 truth calculation. Then we run four experiments with the intermediate resolution configuration ARCTIC025 where we vary the κ_{GM} coefficients that scales the strength of the eddy-induced transport in the GM scheme. In one experiment (ARCTIC025-noGM) we run without the GM scheme. Then in two experiments we use a standard GM scheme scaling (Treguier et al., 1997) and cap the maximum κ_{GM} to either a low value (ARCTIC-lowGM) with $\kappa_{GM} \leq 75$ m^{2}s^{-1}, or a high value (ARCTIC-highGM) with $\kappa_{GM} \leq 2000$ m^{2}s^{-1}. Then in the last experiment we run with the GEOMETRIC scaling and use a capping value

160 $\kappa_{GM} \leq 2000$ m^{2}s^{-1}. The settings are summarised in Table 1, and the time-mean κ_{GM} fields are shown in Figure 3. Clearly the GEOMETRIC scaling gives quite a lot higher κ_{GM} in some regions, e.g., western North Atlantic, south of Iceland, eastern Nordic Seas, and the shelf-break in Canada basin. Observational estimates of surface κ_{GM} (Kusters et al., 2025), based on an inverse method and hydrografic data, show higher values along the western and eastern flanks of the subpolar North Atlantic and lower values in the Nordic Seas. The observational data are very patchy in the Arctic Ocean and presumably the method

165 performs less well there. It is evident that the low κ_{GM} scaling is much smaller than the observations. The high κ_{GM} yields values that are somewhat lower in the subpolar North Atlantic, while the GEOMETRIC scaling mostly yields values that are too high. In the Nordic Seas the high κ_{GM} scaling is quite in line with observations while the GEOMETRIC scaling gives too high values. Here we compare the surface observational data to our κ_{GM} scalings, the observational dataset provides the 3D distribution of κ_{GM} that, in the North Atlantic ocean and high latitudes show a reduction in κ_{GM} with depth in the upper

170 1000 m. Our κ_{GM}, in contrast, lack a vertical structure. As our focus is on the impact of the GM scheme other scalings such
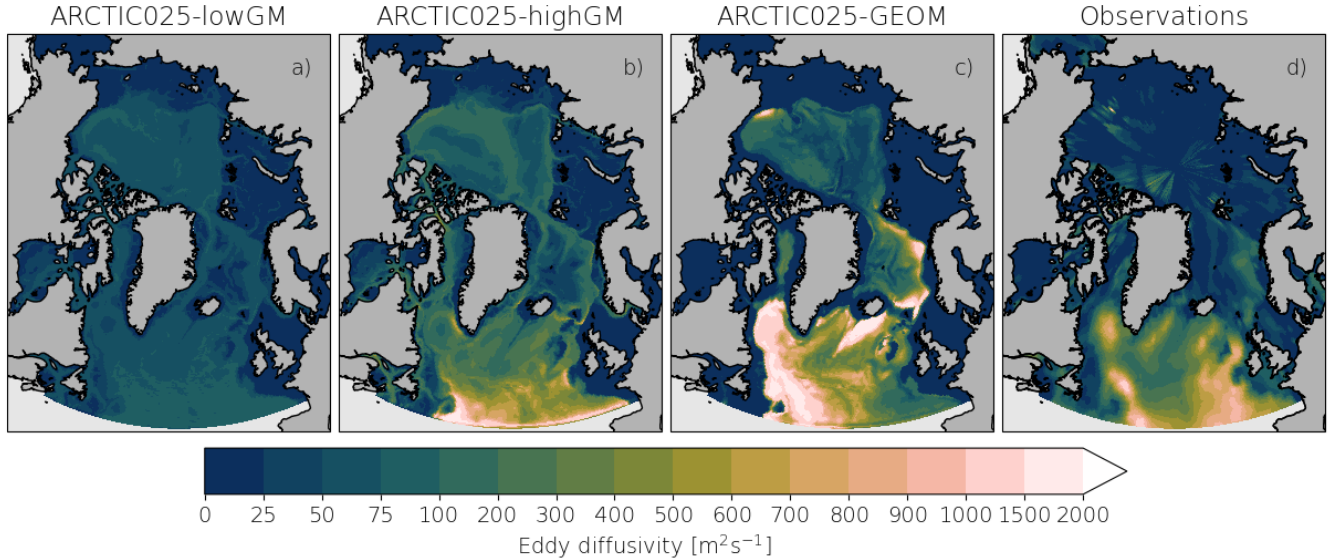
Figure 3. The time-mean (2007–2017) κ_{GM} fields for the a) ARCTIC025-lowGM, b) ARCTIC025-highGM, c) ARCTIC025-GEOM, and d) observational estimate of surface κ_{GM} (Kusters et al., 2025). Note that the color range increases with increasing κ_{GM}.

Table 1. List of experiments used in this study with the domain average horizontal resolution, the domain average κ_{Redi}, and the κ_{GM} capping value used in the GM schemes. Note that the domain ranges are given between the brackets for horizontal resolution and κ_{Redi}, respectively.

Experiment	Horizontal resolution [m]	κ_{Redi} [m^{2}s^{-1}]	κ_{GM} [m^{2}s^{-1}]	Description
ARCTIC12	5 (2–7)	46 (22–66)	-	High resolution experiment without GM
ARCTIC025-noGM	14 (3–20)	136 (54–197)	-	Intermediate resolution experiment without GM
ARCTIC025-lowGM	14 (3–20)	136 (54–197)	< 75	Intermediate resolution experiment with low GM
ARCTIC025-highGM	14 (3–20)	136 (54–197)	< 2000	Intermediate resolution experiment with high GM
ARCTIC025-GEOM	14 (3–20)	136 (54–197)	< 2000	Intermediate resolution experiment with GEOMETRIC

as the lateral viscosity and diffusivity velocity scales U_{visc} and U_{diff} are kept the same between ARCTIC12 and ARCTIC025 configurations when scaling the viscosity and diffusivity (Redi) coefficients, see Table 1.

All experiments also use the same atmospheric and open boundary forcings, and initial conditions. As atmospheric forcing we use 2m air temperature, 2m specific humidity, 10m u/v wind components, shortwave and downwelling longwave radiation, 175 sea level pressure, total precipitation and snowfall with a 3-hourly frequency from the JRA55-do dataset (Tsujino et al., 2018). At the open boundaries we use monthly ORAS5 data (Copernicus Climate Change Service, 2021) for temperature, salinity, sea surface height, barotropic and baroclinic velocities. The experiments are started from an ocean at rest with initial conditions for salinity and temperature taken from the PHC3.0 (Polar science center Hydrographic Climatology, Steele et al., 2001) and sea

ice thickness and concentration from the GLORYS reanalysis (European Union-Copernicus Marine Service, 2018). A monthly
climatology of river runoff from Dai and Trenberth dataset (Dai, 2017) is used. Then we run the experiments for the period
1979–2017 and do most of our analysis on the last ten years (2008–2017). The circulation timescales of AW in the Arctic
Ocean is estimated to be 15–55 years (Wefing et al., 2021) so the experiments are presumably not fully spun up. However,
our main aim here is to compare the effect of the GM parameterization between different experiments with ARCTIC025 and
the high resolution ARCTIC12, so having the first 29 years as spin up should be sufficient to our purpose. In addition, we
will mainly focus our analysis on the flow changes in the Nordic Seas and Eurasian[1] basin which presumably have shorter
circulation timescales.

2.3 Observational data

For many of our metrics we compare the model experiments to observational estimates. Estimates of kinetic energy are taken
from the dataset provide by von Appen et al. (2022). The barotropic circulation is compared to the TOPAZ4 reanalysis from the
Copernicus Marine Services (ARCTIC_MULTIYEAR_PHY_002_003, 2024). Observational estimates for volume transport
across the GSR are described in (Østerhus et al., 2019) and heat transport taken from the dataset provided by Tsubouchi et al.
(2020). Hydrography is compared to the PHC3.0 dataset (Steele et al., 2001). The observational estimates for κ_{GM} are from
the dataset provided by Kusters et al. (2025).

2.4 Model evaluation metrics

To evaluate the model simulations we compute a number of metrics that are briefly described below. To analyse the impact on
energetics we compute the the total kinetic energy (TKE) which can be partitioned into mean kinetic energy (MKE) and eddy
kinetic energy (EKE) using Reynolds decomposition,

$$EKE = TKE - MKE = \frac{1}{2}\left(\bar{u^2} + \bar{v^2}\right) - \frac{1}{2}\left(\bar{u}^2 + \bar{v}^2\right), \tag{3}$$

where u and v are the horizontal velocity components in zonal and meridional directions, and overline denotes the temporal
(monthly) average. Note that with this decomposition the EKE contains energy contributions from all variations on time-scales
shorter than 1 month, not only that contained by the coherent eddies.

To analyse the large-scale circulation we compute the barotropic streamfunction by integrating the barotropic meridional
transport in the zonal direction,

$$\psi_{bt}(x,y,t) = \int\limits_{x_{east}}^{x} \int\limits_{-H}^{\eta} v(x',y,z,t)\,dz\,dx', \tag{4}$$

---

[1]The Eurasian basin includes the Nansen and Amundsen basins, see Figure 1.

where $v(x,y,z,t)$ is the meridional velocity component and H the depth. Then we also compute the meridional overturning circulation (MOC) in depth coordinates as

$$\psi_{MOCz}(y,z,t) = \int_{-H}^{z} \int_{x_{east}}^{x_{west}} v(x,y,z,t)\,dz\,dx. \tag{5}$$

205 The volume and heat transport can be computed as

$$F(t) = \iint_{A} Sv_{\perp}(x,z,t)dA \tag{6}$$

where $v_{\perp}$ is the crossectional velocity, A the crossectional area and S is a factor that is either $S = 1$ for volume transport or $S = c_p\rho_0(\theta - \theta_{ref})$ for heat transport. θ is the potential temperature, $\theta_{ref} = 0.0$ the reference temperature, $c_p = 3992\,J\,K^{-1}\,kg^{-1}$ the specific heat, and $\rho_0 = 1026\,kg\,m^{-3}$ density of seawater. We note that Eq. 6 does not provide the actual heat transport through the section, as that would require a closed volume budget across the section (Schauer and Beszczynska-Möller, 2009).

210 However, to facilitate comparison to observational estimates and other modelling studies we use this common computation of "heat" transport.

3 Results

To understand how both horizontal resolution and the GM scheme impact the circulation and hydrography we now look at a number of different metrics. First we analysis the impact on model energetics by looking at the kinetic energy partitioning.

215 This is followed by an analysis of the barotropic and meridional overturning circulation. Then we look at the volume and heat transport across the key gateways at GSR, Fram Strait and Barents Sea Opening. Finally, we look at the impact on the potential temperature in the AW layer and the hydrography along the AW pathway.

3.1 Partitioning of mean and eddy kinetic energy

First we focus on TKE of the AW layer to see how energetic and eddy active the model configurations are, since this has

220 implications for the redistribution of salt and heat as well as the strength of the boundary current. In Figure 4 the time-mean partitioning of TKE into MKE and EKE in the AW layer (at 623 m depth) is shown. It is evident that both the resolution and the GM scheme impact the MKE as the ARCTIC12 and ARCTIC025-noGM have much higher levels in the Nordic Seas and central Arctic Ocean. The levels are high not only in the boundary current, but also in the basin interiors. The EKE, on the other hand, is generally low in the models, except for the ARCTIC12 that has elevated levels of EKE in the central Norwegian

225 Sea which are about one order of magnitude greater than ARCTIC025 configurations. All configurations show slightly higher levels of EKE along the boundary current pathway and in the Fram Strait region, and lower levels in the interior. This is to some extent in agreement with the observations (Fig. 4k) although the levels are higher in the observations.

To further look at the difference in MKE and EKE we compute the spatial averages at four selected regions along the pathway of the boundary current. Figure 5 shows that the MKE of the boundary current is generally higher in the high resolution
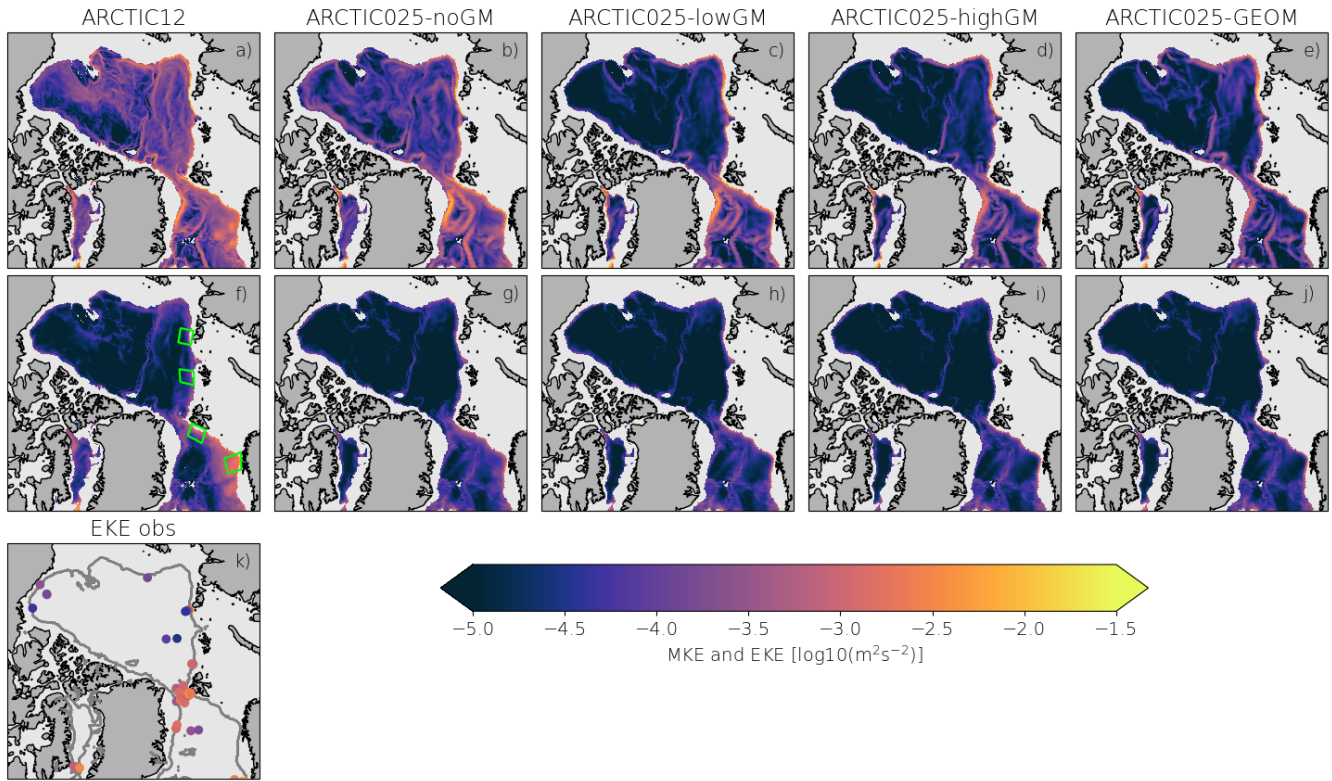
Figure 4. Panels a)–e) show the time-mean (2008–2017) MKE and panels f)–j) the EKE in the AW layer (623 m depth) for the ARCTIC12, ARCTIC025-noGM, ARCTIC025-lowGM, ARCTIC025-highGM, and ARCTIC025-GEOM, respectively. Panel k) shows observations of EKE from von Appen et al. (2022), averaged over the depth range 500–1000m, with the grey line showing the 623 m isobath. The green boxes in panel f) show the regions where the MKE and EKE are averged (presented in Fig. 5).

simulation (ARCTIC12) and is reduced with the GM scheme where ARCTIC025-highGM/ARCTIC025-GEOM (which has the strongest eddy-induced transport) have lower levels. In all experiments the MKE in the boundary current also drops to lower levels when entering the western Nansen basin. Then in the eastern Nansen basin it increase to even higher levels than in the Norwegian Sea and West Spitzbergen Current (WSC). This is presumably due to a more energetic Barents Sea branch that connects to boundary current just upstream at St. Anna Trough. Figure 5 also shows that the partitioning of TKE is quite different between the high resolution and intermediate resolution experiments in the Norwegian Sea region. Here EKE constitutes 57% and 28% of TKE in the ARCTIC12 and ARCTIC025, respectively. Inside the Arctic Ocean (regions WNB and ENB) the contribution of EKE drops off significantly in the high resolution experiments and is on similar levels (5–12% of TKE) as the intermediate resolution experiments. This reflects the drop off in EKE in the basin interior which is seen both in observation and model simulations (Fig 4f–k). The GM scheme also reduces the EKE in the boundary current regions. To

11
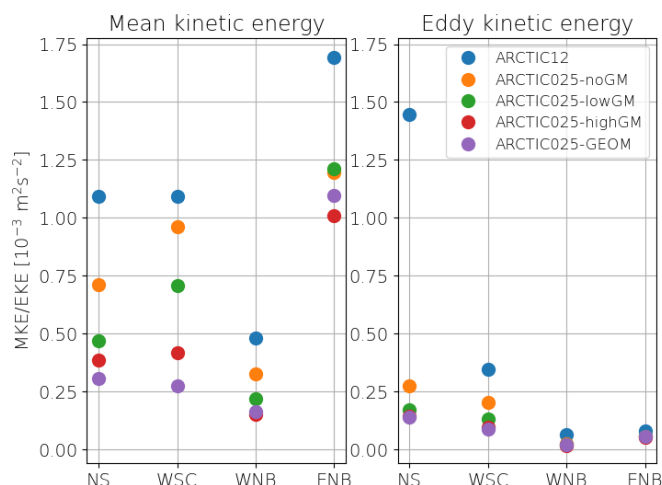
Figure 5. Spatial averages of MKE/EKE at four selected regions along the pathway of the AW boundary current. The regions are NS=Norwegian Sea, WSC=West Spitzbergen Current, WNB=Western Nansen Basin, and ENB=Eastern Nansen Basin, all shown in Figure 4f.

240 further show the drop off in eddy activity between the experiments and the dampening effect of the GM scheme on the resolved eddy field we also show daily snapshots of relative vorticity and potential temperature in Figures A1 and A2.

3.2 Barotropic circulation and the Greenland Sea Gyre

Next, we focus on the large-scale barotropic circulation. Figure 6 shows the time-mean barotropic circulation in the different experiments as well as the Arctic reanalysis TOPAZ4 (from the Copernicus Marine Services, ARCTIC_MULTIYEAR_PHY_002_003,

245 2024). All experiments show a cyclonic circulation over the northern North Atlantic, Nordic Seas and Eurasian basin. Over the Canada basin there is mostly an anticyclonic circulation in all experiments except ARCTIC025-noGM. A similar circulation pattern with cyclonic/anticyclonic circulation is seen in TOPAZ4 as well. ARCTIC025-noGM instead has a weak cyclonic circulation over the Canada basin. The observed upper ocean circulation in the Canada basin tend to be mostly anticyclonic while the circulation in the AW layer is cyclonic (e.g. Rudels et al., 2011). The upper ocean circulation of PSW is dominantly

250 anticyclonic over the Canada basin in all experiments (not shown). This suggests that excluding the GM parameterization leads to a stronger mean AW layer circulation in the intermediate resolution configuration which then dominates the contribution to the vertically integrated barotropic circulation in the Canada basin.

The circulation over the Nordic Seas is dominated by the Greenland Sea Gyre which is stronger in the ARCTIC025-noGM/lowGM than the ARCTIC12 and ARCTIC025-highGM/ARCTIC025-GEOM configurations. Clearly the strength of

255 the barotropic circulation is impacted by the GM scheme and the strength of the eddy-induced transport. This is further seen in Figure 6g that shows the strength of the Greenland Sea Gyre with time. As the model start to adjust to the forcing the response is different between the different configurations. ARCTIC12 and ARCTIC025-highGM adjust to a similar gyre strength (-8.9 Sv
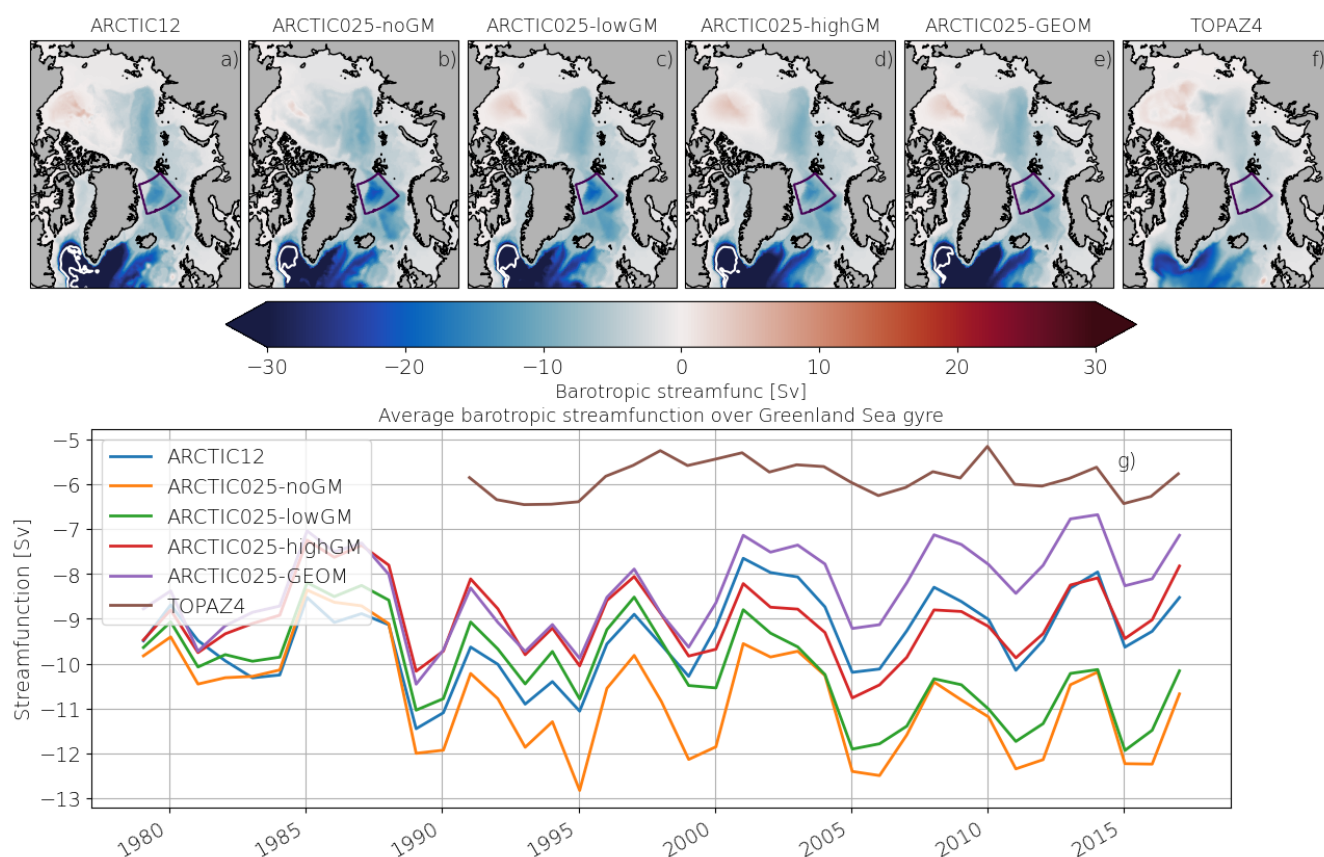
Figure 6. Panels a)–e) show the time-mean (2008–2017) barotropic streamfunction [Sv] for the ARCTIC12, ARCTIC025-noGM, ARCTIC025-lowGM, ARCTIC025-highGM, and ARCTIC025-GEOM, respectively. Panel f) shows the barotropic streamfunction for the TOPAZ4 reanalysis averaged over the same period, and g) show the yearly mean temporal evolution of the spatial averaged barotropic streamfunction. The Greenland Sea Gyre spatial averaging is done over the purple box shown in a)-f), and the white lines show the -45 Sv isoline in the subpolar gyre.

for the period 2008–2017), while the ARCTIC025-GEOM strength is 1.5 Sv weaker and the ARCTIC025-noGM/ARCTIC025-lowGM is 2 Sv stronger. This is stronger than the gyre strength in the TOPAZ4 (-5.9 Sv), but in line with the -8 to -10 Sv

260 range from the multi model study by Muilwijk et al. (2019). However, we note that both TOPAZ4 and most of the models in Muilwijk et al. (2019) use different atmospheric forcing than our experiments which might impact the strength of the gyre.

It is also seen in Figure 6 that the subpolar gyre is stronger in the high resolution simulation. For the time-mean barotropic streamfunction the minimum is -67 Sv in ARCTIC12 and -51, -54, -53, and -49 Sv in ARCTIC025-noGM, ARCTIC025-lowGM, ARCTIC025-highGM, and ARCTIC025-GEOM, respectively. TOPAZ4, in contrast, has a much weaker subpolar gyre

265 with a minimum of -28 Sv. A similar increase in the subpolar gyre strength with resolution has also been reported by Hirschi et al. (2020) where they compare eddy-rich simulations to coarse resolution simulations. However, since the open boundary is very close to the southern extent of the subpolar gyre the results should be interpreted with caution.

3.3 Meridional overturning circulation

To further understand how the resolution and GM scheme impact the circulation in the Nordic Seas we first compute the MOC

270 in depth coordinates (Eq. 5). In Figure 7 we show the time-mean ψ_{MOCz} and maximum overturning in northern North Atlantic and Nordic Seas, which is computed as $max(\psi_{MOCz})$ at 55°N and 73°N, respectively. It is seen that once the simulations have adjusted, the strength of the overturning in the northern North Atlantic Ocean is mostly weaker in the high resolution experiment compared to intermediate resolution experiments (except for ARCTIC025-GEOM). We note that the experiment with a weak eddy-induced transport (ARCTIC-lowGM) has higher overturning than both the ARCTIC-noGM and ARCTIC-

275 highGM experiments. In the Nordic Seas, on the other hand, the high resolution experiment is slightly stronger. There is no evident impact of the GM scheme on the overturning in the Nordic Seas, but in the northern North Atlantic higher eddy-induced transport seems to reduce the overturning.

3.4 Volume and heat transport across the Greenland–Scotland Ridge

The volume and heat transport across the GSR are computed by integrating Eq. 6 over different density intervals using potential

280 density anomalies $\sigma_0 = \rho_0 - 1000$, where ρ_0 is the potential density referenced to surface pressure. Here we distinguish between inflow and overflow water masses using 27.8 kg m^{-3} as the limit at Iceland–Faroe and Denmark Strait gateways and 27.65 kg m^{-3} at Faroe–Scotland. For the Denmark Strait we further sub-divide the lower density range using 27.45 kg m^{-3} to include the outflow water masses that constitutes the buoyant water exported by the East Greenland Current. To close the northward transport to the Nordic Seas we also include the net inflow at Scotland–Norway gateway.

285 The time-mean volume transport across GSR is shown in Figure 8 as well as the summed total inflow, overflow and outflows in Table 2. From Table 2 it is seen that the inflow of AW towards the Nordic Seas across GSR is quite in line with observations for the high resolution experiment ARCTIC12 and the intermediate resolution experiments ARCTIC-noGM and ARCTIC-lowGM, while the experiments with a stronger eddy-induced transport (ARCTIC025-highGM and ARCTIC025-GEOM) have a weaker inflow. The partitioning of the inflow between the different gateways is also different between experiments. At Iceland–

290 Faroe gateway almost all experiments are consistent with observations except ARCTIC025-GEOM which has a much lower
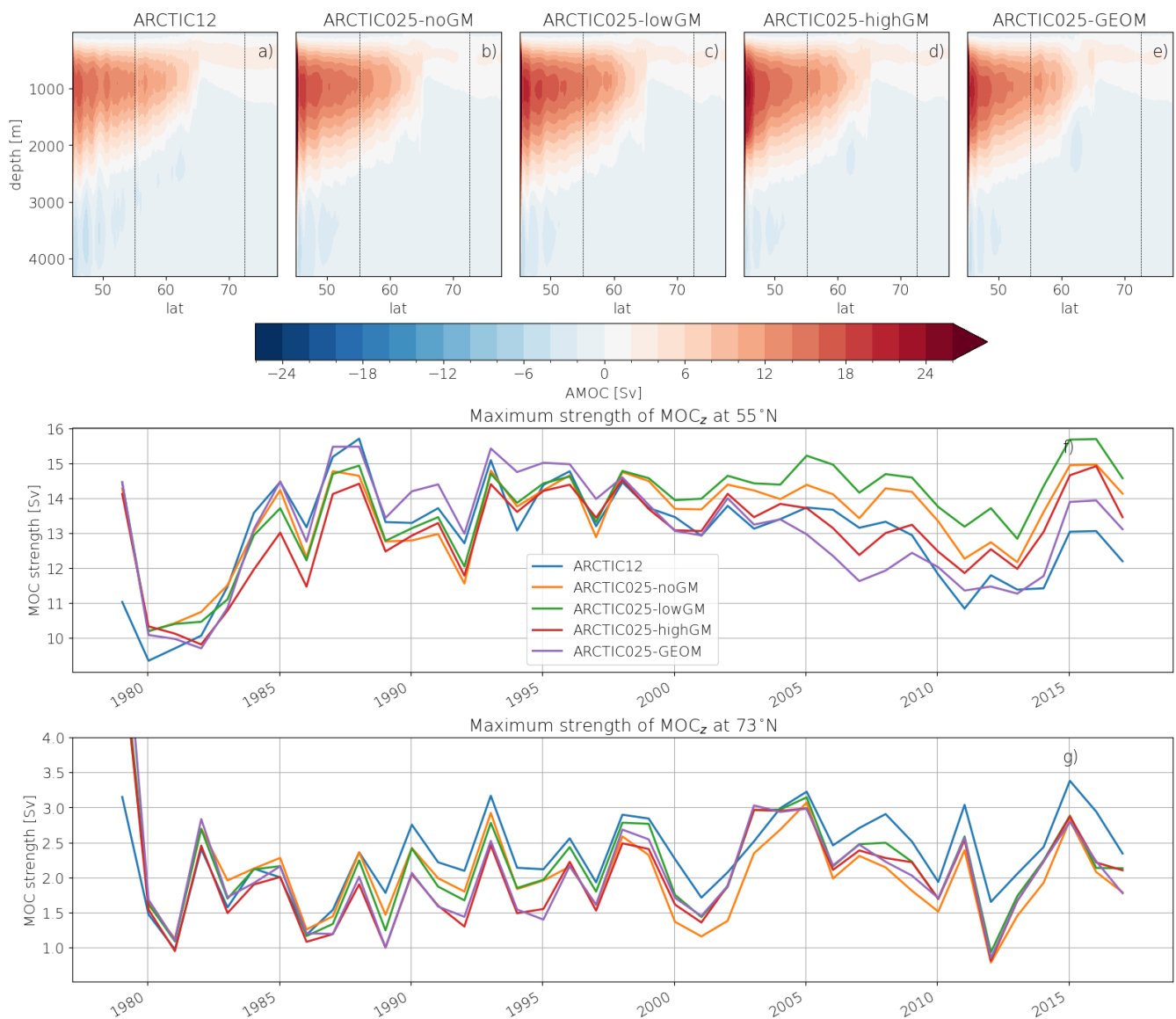
Figure 7. Panels a)–e) show the time-mean (2008–2017) ψ_{MOCz} [Sv] for the ARCTIC12, ARCTIC025-noGM, ARCTIC025-lowGM, ARCTIC025-highGM, and ARCTIC025-GEOM, respectively. Panel f) and g) show the yearly mean temporal evolution of the maximum MOC at approximately 55°N and 73°N, respectively, shown as black vertical lines in panels a)–e).

Table 2. Time-mean (2008–2017) volume transport [Sv] across the Greenland–Scotland Ridge (GSR) which constitutes the Denmark Strait, Iceland–Faroe, and Faroe–Scotland gateways. The transports are divided into inflow and overflow components computed based on density limits. Note that the Denmark Strait gateway also has an additional outflow component that includes less dense water returning southward in the East Greenland Current. We also show the transport across the Scotland–Norway gateway that only has an inflow component. See Figure 1 for the location of the gateways. The Observational estimates are from Østerhus et al. (2019).
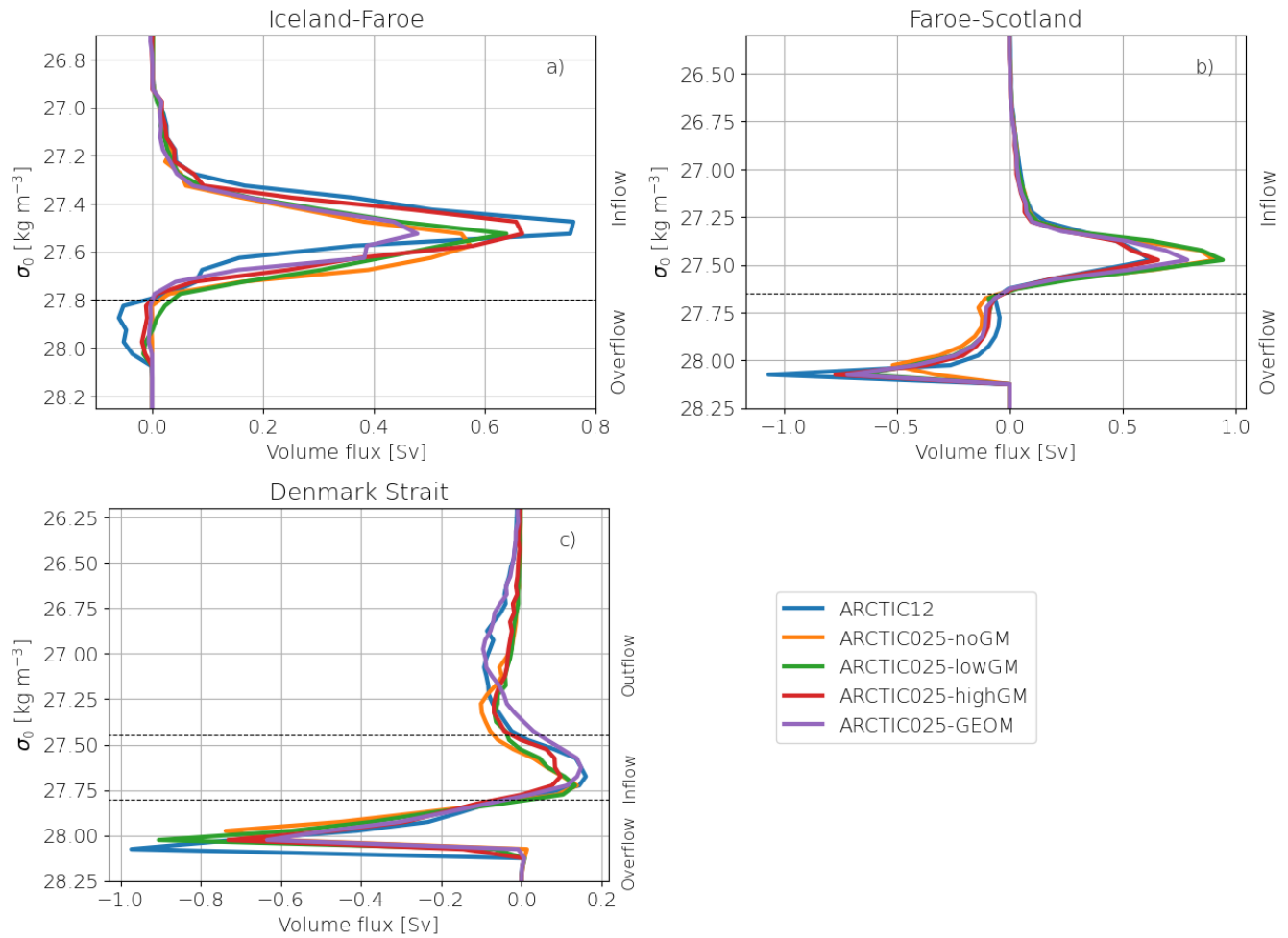
	Iceland-Faroe		Faroe-Scotland		Denmark Strait			GSR		Scotland-Norway
Experiment	Inflow	Overflow	Inflow	Overflow	Inflow	Outflow	Overflow	Inflow	Overflow	Inflow
ARCTIC12	3.7	-0.2	2.9	-1.8	0.7	-1.6	-2.6	7.3	-4.6	0.2
ARCTIC025-noGM	3.5	0.0	3.6	-1.9	0.4	-1.3	-2.1	7.5	-4.0	0.2
ARCTIC025-lowGM	3.4	0.0	3.7	-1.9	0.5	-1.1	-2.2	7.6	-4.1	0.3
ARCTIC025-highGM	3.8	-0.1	2.5	-1.9	0.4	-1.1	-1.9	6.7	-3.9	0.3
ARCTIC025-GEOM	2.7	0.0	2.9	-2.0	0.7	-1.5	-1.7	6.3	-3.7	0.3
Obs	3.8	-0.4	2.7	-2.2	0.9	-2.0	-3.2	7.4	-5.8	0.6

transport. The density of the peak inflow varies between the experiments, with ARCTIC12 and ARCTIC025-highGM shifted towards slightly lower densities (Fig. 8a). At the Faroe–Scotland gateway the inflow in ARCTIC025-noGM and ARCTIC025-lowGM are too strong and the ARCTIC025-highGM slightly to weak. At Denmark Strait both the inflows and outflows are slightly stronger in ARCTIC12 and ARCTIC025-GEOM compared to the other experiments, but weaker than observations.

295 However, as seen in Figure 8 the shift from a net inflow to outflow is not well-defined with a fixed density limit, so the results should be interpreted with caution. We also note that all experiments have a much weaker inflow at the Scotland–Norway gateway compared to observations. However, the observational estimates from Østerhus et al. (2019) includes the contribution of the inflow on the Scottish shelf (they estimated it to be $0.4 - 0.5$ Sv). In our analysis this contribution is instead included in the Faroe–Scotland gateway making our Scotland–Norway inflow lower.

300 Also the overflow across the GSR is weaker in all experiments compared to the observational estimate. Here the high resolution experiment stands out with a stronger overflow compared to the intermediate resolution counterparts, possibly due to better resolving the channels of the gateways. Especially in the Denmark Strait the overflow seems to be much weaker in the intermediate resolution experiments. For ARCTIC025 experiments the peak overflow density is slightly lower than high resolution ARCTIC12 (Fig. 8c). Also for the GSR overflow there seems to be an impact of the GM scheme with ARCTIC025-

305 highGM and ARCTIC025-GEOM having weaker overflows.

The northward heat transport that AW carries across the GSR is computed the same limiting densities as for the volume transports. Here we only report the AW inflows at the three main gateways (Iceland–Faroe, Faroe–Scotland and Denmark Strait) that are presented in Table 3. The total northward heat transport in the experiments are consistent with the volume transport in that the intermediate experiments with no or weak eddy-induced transport (ARCTIC025-noGM and ARCTIC025-

310 lowGM) has a higher inflow compared to the experiments with strong eddy-induced transport (ARCTIC025-highGM and

Figure 8. Time-mean (2008–2017) volume transport across the Greenland–Scotland Ridge, here binned into density classes for the separate gateways Iceland–Faroe (a), Faroe–Scotland (b), and Denmark Strait (c). The thin dash and dotted lines show in- and outflow, respectively; and the solid line the netflow. The dash black horizontal lines show limiting densities for computing inflows and overflows (and outflows for Denmarks Strait).

Table 3. Time-mean (2008–2017) northward heat transport [TW] across GSR. See Figure 1 for the location of the gateways. The observational estimates are from Tsubouchi et al. (2020).

	Iceland-Faroe	Faroe-Scotland	Denmark Strait	GSR
ARCTIC12	136	135	33	305
ARCTIC025-noGM	116	169	27	312
ARCTIC025-lowGM	116	177	29	322
ARCTIC025-highGM	136	133	23	293
ARCTIC025-GEOM	96	149	25	271
Obs	126	125	26	277

ARCTIC025-GEOM), and the high resolution experiment is somewhere in between. Here the ARCTIC025-GEOM are closest to observational estimates., while the other experiments overestimate the northward heat transport across GSR. We also note that the ARCTIC12 and ARCTIC-highGM have an equal partitioning of the heat transport between the Iceland–Faroe and Faroe–Scotland gateways, similar to observations. While the other experiments have a weaker (stronger) heat transport through
315   the Iceland–Faroe (Faroe–Scotland) gateway.

3.5 Volume and heat transport across the Barents Sea Opening and Fram Strait

Next we consider the exchange between the Nordic Seas and the Arctic Ocean by looking at the time-mean volume and heat transports across the Barents Sea Opening (BSO) and Fram Strait (Table 4). Note that here we compute the transport over the whole water column rather than separating it into different density classes as we did for GSR. It is seen that the net volume
320   transport across BSO is slightly stronger in the high resolution experiment than in the intermediate resolution experiments. The in- and outflows, however, are much stronger (more than 1 Sv higher in each direction) in the high resolution experiment. Table 4 also shows that the effect of the GM parameterization is quite modest on the volume transport across BSO. Compared to observations all model experiments have higher net volume transport than the 2.0 Sv estimated by Smedsrud et al. (2010), but lower than the 3.6 Sv inverse model estimate by Tsubouchi et al. (2012). Although the in- and outflows in the model
325   experiments are higher than estimates reported Tsubouchi et al. (2012). The northward heat transport also show that the high resolution gives a stronger northward heat flux compared to intermediate resolution experiments, and that all model experiments have higher heat flux than the inverse model estimate by Tsubouchi et al. (2012). Our experiments show an increase in both the net volume and northward heat transport across BSO with time (not shown), which is also consistent with model simulations by Muilwijk et al. (2018). The positive trend in transport across BSO can presumably explain some part of the higher values in
330   our experiments compared to estimates by Tsubouchi et al. (2012) which only represents summer 2005 values.

In the Fram Strait (Table 4) the net volume transport is dominated by a southward flow in all experiments. It is further seen that the high resolution experiments have a much stronger net, and in- and outflows compared to the intermediate resolution experiments. The intermediate resolution experiments also show that, in contrast to the BSO, the volume transport at Fram

Table 4. Time-mean (2008–2017) volume [Sv] and heat [TW] transport across the Barents Sea Opening and Fram Strait. A positive volume transport means a northward flow towards the Arctic Ocean. For the heat transport we only report the northward 'in' component. See Figure 1 for the location of the gateways.

| | Volume transport | | | | | | Heat transport | |
| | Barents Sea Opening | | | Fram Strait | | | Barents Sea Opening | Fram Strait |
	Net	In	Out	Net	In	Out	In	In
ARCTIC12	3.2	5.9	−2.7	−1.8	7.2	−9.1	152	71
ARCTIC025-noGM	2.9	4.4	−1.6	−0.5	6.2	−6.7	112	64
ARCTIC025-lowGM	3.0	4.6	−1.6	−0.3	5.2	−5.6	117	54
ARCTIC025-highGM	2.9	4.4	−1.5	−1.0	4.2	−5.2	110	38
ARCTIC025-GEOM	3.0	4.4	−1.5	−1.6	4.4	−6.0	111	33
Obs	2.0[a], 3.6[b]	3.2[a]	−1.2[a]	−1.6[b], −2.0[c]	4.1[b]	−5.8[b]	103[b]	44[bd]

[a]Smedsrud et al. (2010)
[b]Tsubouchi et al. (2012)
[c]Schauer et al. (2008)
[d]Rudels et al. (2015)

Strait seems to be impacted by the GM parameterization. Here the experiments with a strong eddy-induced transport have a stronger net southward transport. This is mainly due to weaker inflows in ARCTIC025-highGM/ARCTIC025-GEOM than the ARCTIC025-lowGM experiment, and particularly the ARCTIC025-noGM experiment. We also note that for the experiments with strong eddy-induced transport the GEOMETRIC scheme gives a stronger southward flow than the standard GM formulation. The weaker northward volume transport also lead to reduced heat transport into the Arctic Ocean in experiments with strong eddy-induced transport, and the high resolution experiment has a larger heat transport compared to the intermediate resolution experiments.

Comparing simulated transports to observational estimates at the Fram Strait can be challenging since the observations are not covering the entire strait due to the severe ice conditions on the east Greenland shelf, and due to a recirculation in the strait where parts of the northward flowing AW recirculates southward (Marnela et al., 2013). However, our simulations show that the high resolution experiment has a net southward exchange (−1.8 Sv) that is within the range of observational estimates (−2.0 to −1.6 Sv), while the intermediate resolution experiments, except ARCTIC025-GEOM, underestimates the net southward transport. However, even though the high resolution experiment agrees well with the net volume transport estimated by Tsubouchi et al. (2012), both the in- and outflows are much larger, whereas the ARCTIC025-GEOM in- and outflows are closer to observations.

The northward heat transport in the Fram Strait is more or less half of that in BSO in observations as well as all the model experiments. The high resolution experiment gives the largest northward heat transport followed by ARCTIC025-noGM and ARCTIC025-lowGM, which all have higher net heat transports than estimated by Rudels et al. (2015) from observations for

the years 2007 and 2011. The remaining model experiments (ARCTIC025-highGM and ARCTIC025-GEOM) have somewhat lower heat fluxes than in Rudels et al. (2015) but higher than the average estimation at 79° N of Marnela et al. (2013, 30.4 ± 10.5 TW). As mentioned before comparing with observations can be challenging, especially for heat fluxes where the reference temperature is somewhat arbitrary (Schauer et al., 2008). Using a stream tube approach Schauer et al. (2008) show that the net heat transport varies from 26–50 TW between 1999 and 2007 with an uncertainty estimate of ± 6 TW.

3.6 Hydrographic and velocity structure at the Fram Strait

The Fram Strait is the deepest gateway to the Arctic Ocean and an important pathway for the water mass exchange between the Arctic Ocean and North Atlantic Ocean. To further see the impact of the resolution and the GM parameterization on the circulation and water mass exchange we show the potential temperature, density and crossectional current speed in Figure 9. We focus on the water masses and flow of the upper 1000 m. Here the flow is expected to be dominated by northward flowing AW in WSC on the eastern flank of the strait and recirculating AW in WSC situated more centrally in the strait. On the western flank we expect southward flowing PSW in East Greenland Current (EGC), and returning AW below the EGC, that has been cooled slightly on its path circulating around the Arctic Ocean (e.g. Beszczynska-Möller et al., 2012).

The potential temperature structure in the experiments (Fig 9 a–e) reveal a core of warm ($T > 3°$ C) AW in the WSC that is clearly warmer and more buoyant in the experiments with weak eddy-induced transport (ARCTIC025-noGM/ARCTIC025-lowGM). In the ARCTIC025-noGM the warm AW core extends over almost the entire strait at depths $0 - 750$ m. In the upper western part of the strait there is a well-defined cold ($T < 0°$ C) water mass of PSW, which is somewhat shallower in experiments ARCTIC025-noGM/ARCTIC025-lowGM. Below the PSW there is also returning AW with slightly warmer ($0 < T < 3°$ C) temperatures. It is also seen that isopycnals in experiments with strong eddy-induced transport (ARCTIC025-highGM/ARCTIC025-GEOM) are more flattened than the experiments with weak eddy-induced transport, as expected.

The crossectional current in the experiments also share similar features (Fig 9 f–j). On the eastern flank of the strait all experiments show a narrow and distinct northward WSC shelf branch next to Svalbard and an outer offshore WSC branch centred around longitude $5°$ E. On the western flank there is well-defined southward flowing EGC just off the shelf break of both colder PSW and warmer AW slightly below. There is also a recirculation of PSW on the eastern Greenland shelf. In the central parts, on the other hand, the high resolution experiment has a different structure compared to intermediate resolution experiments showing signs of a more distinct recirculation of AW in the strait. The crossectional current is also stronger in the high resolution experiment, consistent with the stronger bi-directional flow in Table 4, and with a more surface intensified baroclinic structure in both the in- and outflows. The GM scheme impact particularly the vertical structure of the outflowing water with stronger currents in the deeper parts (below 500 m) in ARCTIC025-noGM/ARCTIC025-lowGM configurations compared to ARCTIC025-highGM. Interestingly the ARCTIC025-GEOM show a different vertical structure with stronger outflow in the upper 1500 meter compared to the other ARCTIC025 configurations.
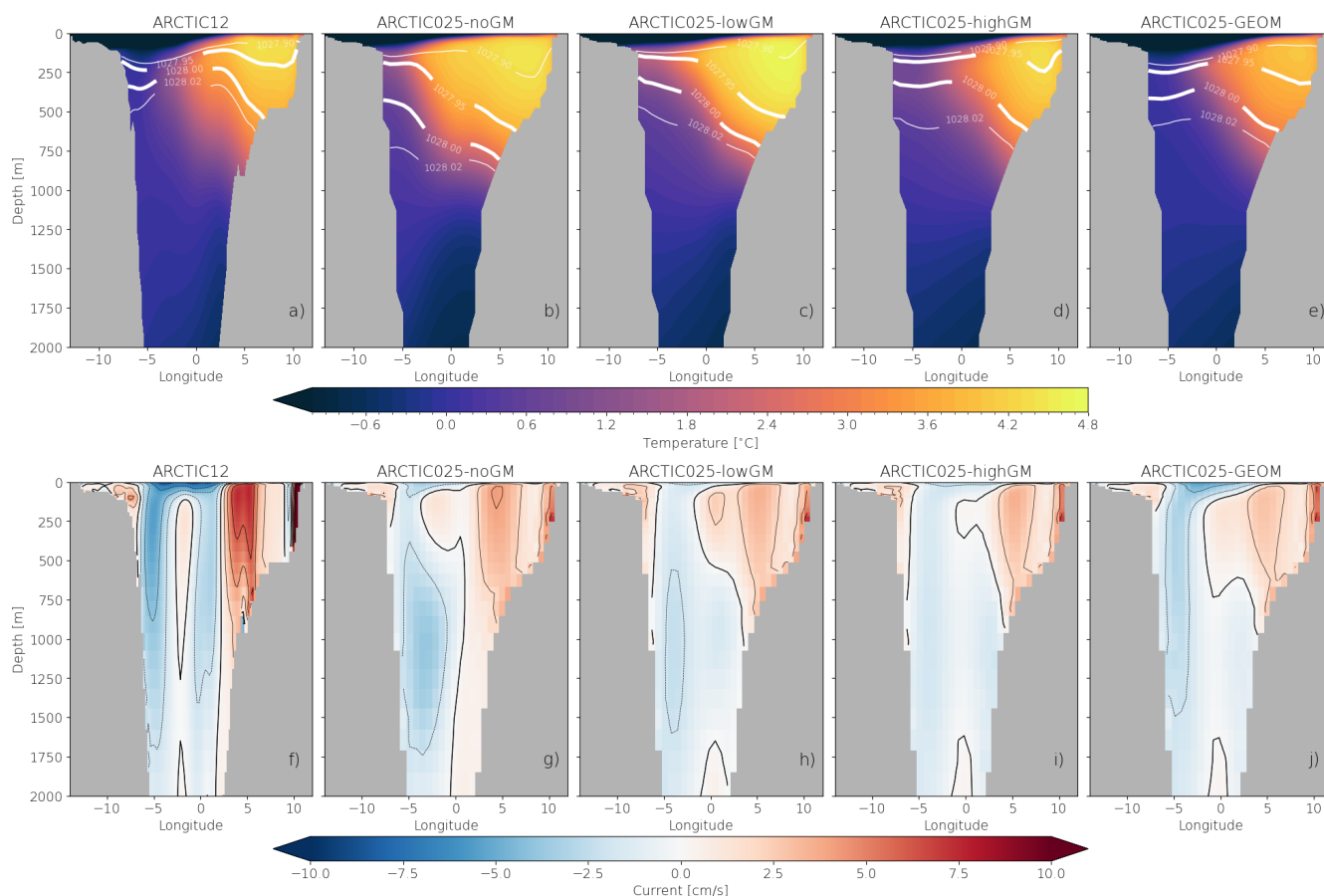
Figure 9. Fram Strait potential temperature, density (a–e) and crosssectional current (f–j) averaged over the period 2008–2017.

3.7 Atlantic Water layer temperature

To assess the simulated temperature in the AW layer in the different experiments we compare the model experiment with the
PHC3.0 climatology (Steele et al., 2001). Observations show that in the Nordic Seas the warmest temperatures are found close
to the surface while in the Arctic Ocean the core of the AW layer (where the temperature maximum T_{max} is found) is situated
somewhere between $100 - 800$ meter. The depth of the AW layer core typical deepens from 250 meter in the Nansen basin to
$300 - 400$ meter in the Amundsen, Makarov and Canada basins (e.g. Timmermans and Marshall, 2020). Here we select the
model level that equals 233 meter, which thus mainly represent the AW layer core temperature in the Nansen basin. Selecting
deeper levels in the model show qualitatively similar results.

Figure 10 shows the time-mean AW layer potential temperature from the model simulations and the PHC3.0 climatology.
It is seen that the model experiments are warmer than PHC3.0 in the Nordic Seas, Barents Sea and western Nansen basin. In
the Amundsen basin, on the other hand, ARCTIC12, ARCTIC025-lowGM, ARCTIC025-highGM, and ARCTIC025-GEOM
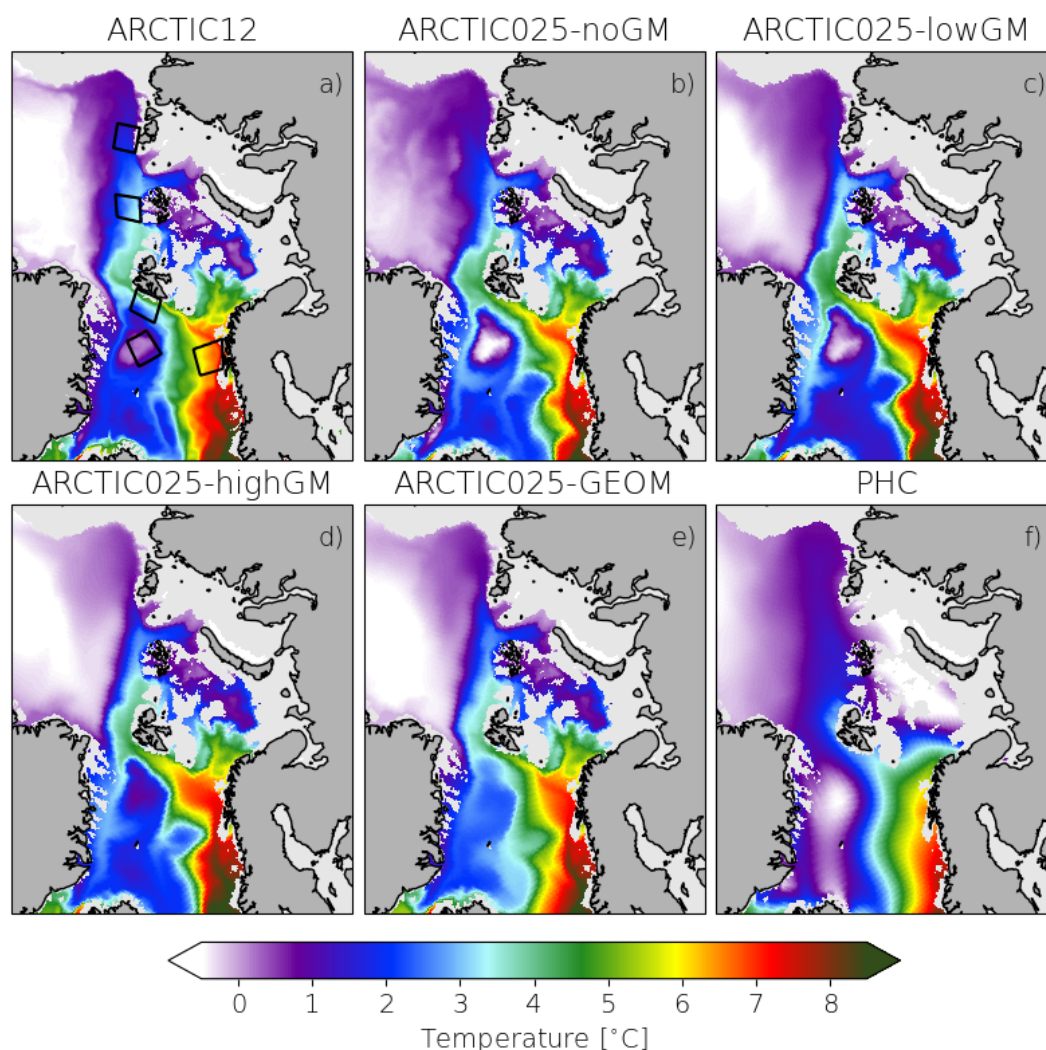
Figure 10. Time-mean (2008–2017) potential temperature in the AW layer (233 m depth) averaged over the period 2008–2017 for the different experiments. Black boxes show in panel a) the sub-regions Norwegian Sea, West Spitzbergen Current, Greenland Sea, Western Nansen basin, and Eastern Nansen basin, where vertical profiles (shown in Figs. 11 and 12 below) are computed.

all have colder temperatures. It should also be noted that PHC3.0 is quite coarse and only represents the large-scale structures

395   of the temperature distribution. In addition, the observations mainly represents conditions from the 1970s to 2000s meaning that we expected the simulated temperature to be warmer as they represent a later period where we have seen a warming of the northward flowing AW (Polyakov et al., 2023; Smedsrud et al., 2022). Nevertheless, comparing to PHC3.0 still reveals valuable information on the lateral AW temperature gradients across the Nordic Seas and Arctic Ocean.

The GM scheme clearly impacts the potential temperature distribution in the Nordic Seas. The experiments with the GM
400 scheme activated have a wider boundary current region with warmer temperatures in northern Norwegian Sea. In the Green-
land Sea the high resolution experiment and the intermediate resolution experiment with weak eddy-induced or no transport
(ARCTIC025-noGM and ARCTIC025-lowGM) as well as PHC3.0 show a colder region in the central parts. However, the
experiments with strong eddy-induced transport (ARCTIC025-highGM, and particularly ARCTIC025-GEOM) are generally
warmer here implying too strong lateral heat transport between the boundary current and the basin interior.

405 The snapshots of potential temperature (Fig A2) show that more warm water eddies are shedding off the boundary current in
the high resolution experiment and in the experiment without GM. However, the impact of the GM scheme and the resolution on
time-mean temperature distributions (Fig 10) in the Arctic Ocean is less obvious. In the western Nansen basin all experiments
show a similar distribution although the width of the warm AW in the boundary current varies somewhat. In the eastern
Nansen basin the temperature distributions vary more with the high resolution experiment generally than the intermediate
410 resolution experiments. As stated earlier all but the ARCTIC025-noGM share a similar distribution of slightly colder water
in the Amundsen basin. In the Barents and Kara seas all experiments show similar temperature distributions implying little
sensitivity to both resolution change and eddy parameterization here.

3.8 Mean hydrography along the Atlantic Water pathway

To further understand the changes of northward flowing AW we have computed spatially averaged vertical profiles of potential
415 temperature and salinity at a few selected regions along the AW pathway (see Fig. 10a for the locations). Figure 11 shows the
time-mean potential temperature and salinity at the selected regions in the northern Nordic Seas. In the northern Norwegian
Sea all experiments are warmer and saltier in the upper 400 m, as expected. The ARCTIC-noGM is slightly colder and less
salty than the other experiments. Between 400–1000 m intermediate resolution experiments tend to become slightly colder
than PHC3.0, implying the resolution impacts the strength of the temperature stratification here. The ARCTIC025-noGM
420 experiment is slightly colder and less salty in this region.

In the WSC region all experiments are warmer and saltier than PHC3.0 throughout the water column. Here the ARCTIC12
and ARCTIC025-GEOM are slightly colder than the other experiment suggesting that GEOMETRIC scheme parameterized
the resolved eddy fluxes better than the standard GM scheme. In Figure 3c it is also seen that the GEOMETRIC scheme has
much higher GM diffusivity values in the WSC region than the standard scaling, although the values are also much higher than
425 the observed values.

In the central Greenland Sea the experiments show a greater variety in their temperature and salinity distribution relative
to PHC3.0. In the upper 100 m the ARCTIC12 and ARCTIC025-GEOM experiments are colder and fresher than PHC3.0
and suggests a more pronounced interaction with the cold and fresh EGC in these experiments. Below 100 m and throughout
the water column all experiments are warmer and saltier than the PHC3.0 climatology. Strehl et al. (2024) show that based
430 on 70 years of observations in the Greenland Sea there has been an increase in temperature and salinity the last decades at
intermediate depths, in line with our experiments. Here the experiments with strong eddy-induced transport, ARCTIC025-
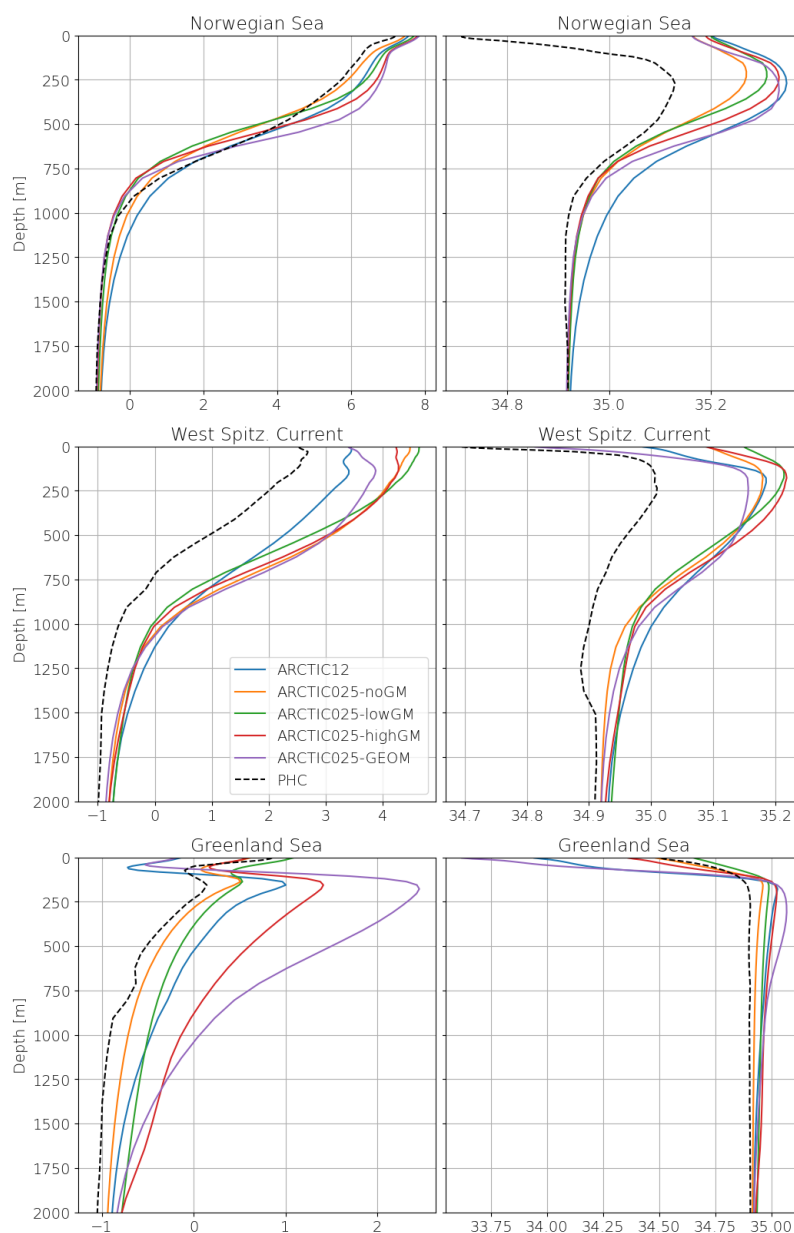
Figure 11. Vertical profiles of time-mean (2008–2017) potential temperature and salinity spatially averaged over regions along the AW pathway. The regions are located in the northern Norwegian Sea, West Spitzbergen Current, and central Greenland Sea, and shown as black boxes in Fig 10a.

highGM, and particularly ARCTIC025-GEOM, are much warmer than the other experiments (as was also seen in Fig. 10) implying too strong lateral heat transport between the boundary current and interior parts.
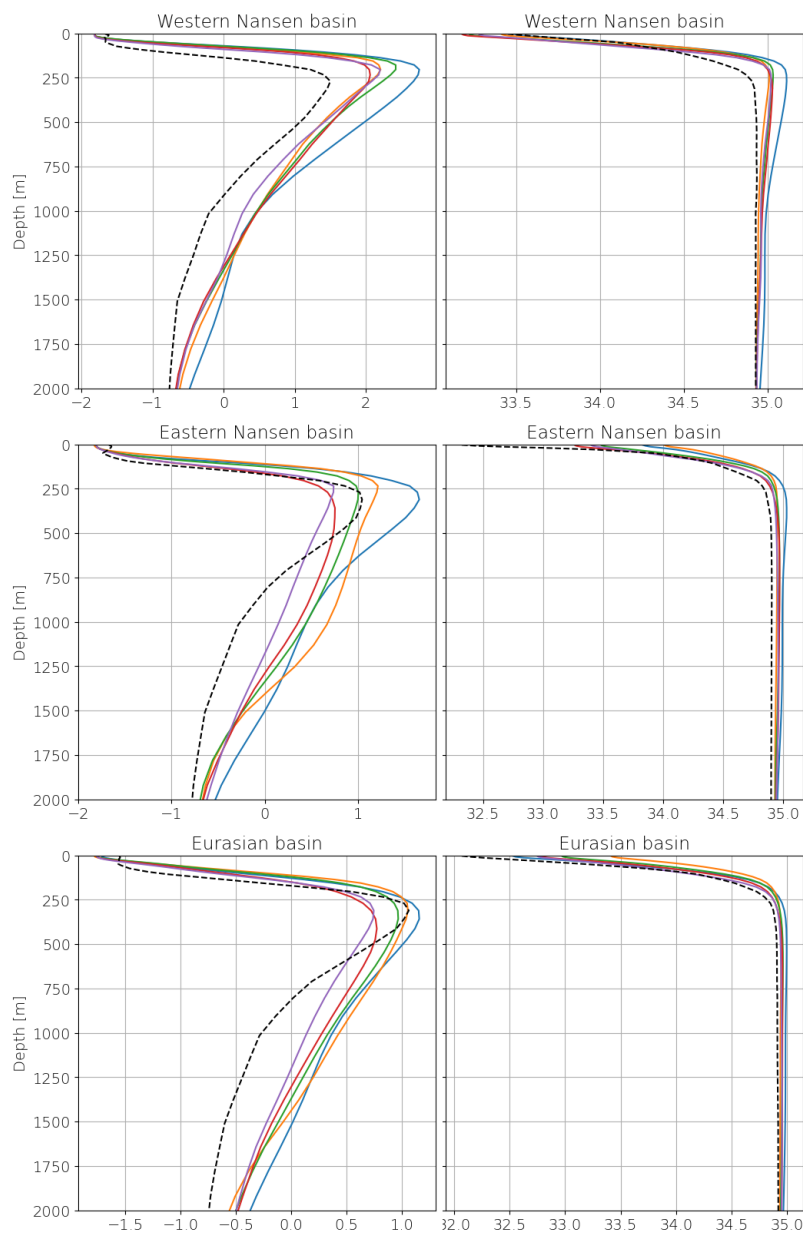
In the western Nansen basin (Fig. 12) all experiments again show a more uniform differences relative to PHC3.0, all being
435   warmer and saltier. The T_{max} in the AW layer ranges from $2.2 - 2.8°$C in the experiments, while PHC show $1.5°$C. The depth of the T_{max} is slightly shallower in all experiments, located at $200 - 230$ m depth, compared to 270 for PHC3.0. Using the thickness of the layer with $T > 0°$C as a measure of AW layer thickness yields $1200 - 1300$ m for the experiments and 800 m for PHC3.0. It is mostly in the bottom of the AW layer that the experiments are thicker than the climatology. What really stands out in this region is that the high resolution experiment is warmer in the AW layer. This agrees with the higher northward heat
440   flux for ARCTIC12 shown in Table 4, and suggests that resolution has an important role in setting the heat import to the Arctic Ocean.

In the eastern Nansen basin the experiments again show a greater variety in particularly their temperature distribution relative to PHC3.0. The high resolution experiment is still warmer but saltier and maintains a similar shape of the vertical temperature profile compared to PHC3.0. The shapes of the intermediate resolution experiments, in contrast, are more flattened in the
445   vertical due to a cooling at the depth of the T_{max} in the AW layer. Here T_{max} ranges from $0.7 - 1.7°$C in the experiments, while PHC show $1.0°$C. Both experiments with a strong eddy-induced transport are colder than PHC3.0. The depth of T_{max} is also more varied ranging from $230 - 360$ with the ARCTIC025-highGM having the deepest T_{max}. The depth of T_{max} in the high resolution experiment is exactly in line with the PHC3.0 at 310 m. Despite the change in vertical structure for the intermediate resolution experiments the thickness of the AW layer is still much thicker in the experiments $(1000 - 1300)$ than
450   PHC3.0 (600 m).

For comparison with earlier studies we also provide vertical profiles averaged over the entire Eurasian basin (Fig. 12). The results are qualitatively similar to the Nansen basin sub-regions in that the high resolution experiment has a warmer T_{max} of $1.2°$ compared to the intermediate resolution experiments with T_{max} in the range $0.8 - 1.1°$, while PHC3.0 has a T_{max} of $1.1°$. It is also seen that the experiments with eddy-induced transport has lower T_{max}, that is significantly colder than PHC3.0. Also
455   in the entire Eurasian basin is the AW layer thickness over estimated with model experiments showing $980 - 1370$ compared to 630 in PHC3.0. Compared to assessment of CMIP6 models presented in Khosravi et al. (2022) and Heuzé et al. (2023) we note that all our experiments show an improved representation of particularly the vertical temperature structure. This is likely an impact of the higher resolution in our experiments. Similar improvements have been reported in Wang et al. (2024) where they compare temperature and salinity structures in several pairs of high and low resolution model configurations.

460   ## 4   Summary and conclusions

We have studied how the GM parameterization impact the eddy-permitting regime in an ocean model. We focused on its effect on the northward flow of AW in the Nordic Seas and Arctic Ocean. Through a set of experiments with an intermediate resolution (eddy-permitting) model configuration we varied the strength of the eddy-induced transport by scaling the GM diffusivity coefficient. We also tested two different GM diffusivity scalings, the commonly used scaling by Treguier et al.

Figure 12. Same as Fig. 11 but for regions located in the western and eastern Nansen basin. We also show the vertical profiles of the entire Eurasian basin.

465   (1997), and the new GEOMETRIC scaling by Mak et al. (2018). The intermediate resolution experiments were then compared
to both observational estimates and a high resolution (eddy-permitting to eddy-resolving) configuration that served as a "model
truth" calculation. To gauge the effect we analysed the impact on the total kinetic energy partitioning, the barotropic and
meridional overturning circulations, the volume and heat transport across the key gateways at GSR, Fram Strait and Barents
Sea Opening, the potential temperature in the AW layer, and the hydrography along the AW pathway.

470   We find that using the GM parameterization in the eddy-permitting intermediate resolution experiments leads to reduced
MKE and EKE in the boundary currents and weaker cyclonic barotropic circulation in the Nordic Seas. As expected GM
dampens the resolved eddy field which impact both the dynamics and tracer distributions. The meridional overturning is
weaker in the northern North Atlantic using GM, however, no sensitivity is seen in the Nordic Seas overturning. The weaker
circulation, in turn, gives reduced northward volume and heat transport across GSR and Fram Strait, while the transport across
475   the Barents Sea Opening shows less sensitivity to the GM parameterization. In addition, the partitioning between the different
gateways at GSR of the inflow is more realistic in our experiments with GM.

The response on the hydrography is somewhat mixed. In the Nordic Seas the use of GM generally yields warmer temper-
atures in the interior parts. For the intermediate resolution configuration, this leads to that the Norwegian Sea being more in
line with the high resolution experiment. This implies that the resolved eddy fluxes are not strong enough to redistribute the
480   heat from the boundary current to the interior if GM is omitted in the intermediate resolution configuration. In the Greenland
Sea, on the other hand, the tracer transport between the boundary current and the interior is too strong leading to a too warm
and salty upper ocean possibly impacting deepwater convection. In the Fram Strait region where the flow is very dynamic
due to both high eddy activity, recirculation and complex topography omitting the GM scheme yields too wide AW core and
weaker net volume transport. Inside the Arctic Ocean the Arctic AW temperature distribution shows less sensitivity to the GM
485   parameterization. Compared to the observed AW layer thickness our model configurations still suffer from a too thick AW
layer. However, the temperature structure is generally improved compared to most CMIP6 models shown in previous model
assessments (Khosravi et al., 2022; Shu et al., 2023; Heuzé et al., 2023).

Further, we studied how the strength of the eddy-induced transport impact the AW circulation by using high and low values of
the GM diffusivity coefficient. A weak eddy-induced transport in our simulations in some cases leads to a response in between
490   no or a strong eddy-induced transport. However, in other cases the response is not between the two extremes, e.g. the GSR
inflow is higher with a small GM coefficient (ARCTIC025-lowGM) than without (ARCTIC025-noGM), while using a large
coefficient (ARCTIC025-highGM) leads to weaker response. We do not have an explanation for this, but a thorough diagnosis
of the energy cycle (e.g. Loose et al., 2022) might shed some light on this, however, detailing the underlying mechanism is a
cumbersome task and out of the scope of the present work. Regardless of the cause, it is clear that setting the strength of the
495   GM coefficient can lead to unintuitive results.

We also compared two different GM diffusivity scalings (standard and GEOMETRIC), both with a high GM diffusivity.
They generally show similar responses which are distinctly different compared to using GM with a low diffusivity or not using
GM. Their spatial GM diffusivity distributions differs substantially with the GEOMETRIC scaling having larger diffusivities
in the western North Atlantic, south of Iceland and eastern Nordic Seas than the standard GM scaling. This impacts the

500 circulation with a weaker Nordic Seas barotropic circulation, northern North Atlantic meridional overturning and northward volume and heat transport across GSR. At Fram Strait the GEOMETRIC scaling, on the other hand, gives a stronger net export out of the Arctic Ocean, in line with observations. The temperature is also warmer in the Nordic Seas and slightly colder in the Eurasian basin with the GEOMETRIC scaling. It should be noted that we did not spend a great deal of effort to tune the new GEOMETRIC scheme. Another point to make is that both scaling used here only have a two-dimensional structure

505 while observational estimates by Kusters et al. (2025) show that the GM diffusivities have a vertical structure with reduction of diffusivities with depth in some regions. Since the GM diffusivities sets the strength of the eddy-induced transport the lack of vertical structure is a missing piece in current implementations.

In addition, our study shows the impact of resolution on the Arctic AW circulation. When resolution is increased we get higher levels of MKE and EKE particularly along the AW pathway. The barotropic circulation over the Nordic Sea and the

510 northern North Atlantic meridional overturning are reduced when resolution is increased. The strength of these circulation metrics are similar to the experiments with high eddy-induced transport showing that the intermediate resolution experiments require some parameterized mesoscale eddy fluxes to capture the missing resolved eddy fluxes. The increase in resolution also leads to improved transport across GSR and the Fram Strait, however, the bi-directional flow in the Fram Strait gets too strong compared to observational estimates. The lateral and vertical temperature distribution are also improved. In the Nordic Seas

515 the eddy dynamics in the high resolution experiment leads to increased lateral eddy heat fluxes in the Norwegian Sea, while the circulation in the Greenland Sea gives less eddy shedding from the boundary current maintaining the cold region in the central Greenland Sea. In a multi-model assessment Wang et al. (2024) also found improvements in Fram Strait transport and Arctic temperature distributions when resolution is increased. Similar improvements in North Atlantic ocean heat transport are also seen in the multi-model study by Docquier et al. (2019).

520 Finally, our study demonstrate the challenges of using the GM parameterization in the eddy-permitting regime. Consistent with earlier idealized studies (Mak et al., 2023; Ruan et al., 2024), we find that omitting the GM parameterization excludes important eddy–mean flow interactions, which in our case results in overly strong North Atlantic meridional overturning, Nordic Seas barotropic circulation, and northward volume and heat transport. On the other hand, applying GM dampens the resolved eddy fluxes, while the parameterized fluxes introduce biases in some regions, particularly in the temperature

525 distribution in the Greenland Sea. The best avenue for the next generation of CMIP climate models to further improve the Arctic Ocean circulation and water mass representation is likely to employ energy consistent and scale-aware GM methods (e.g. Bachman, 2019; Jansen et al., 2019; Mak et al., 2023).

Code availability. The NEMO 4.0.4 code is available under the repository https://svn-mirror.nemo-ocean.eu/NEMO/releases/r4.0/r4.0.4/. The GEOMETRIC code can be found under https://github.com/julianmak/GEOMETRIC_code/tree/main/nemo4.0.5-14538.

Author contributions. PP: conceptualization, formal analysis, methodology, visualization, writing (original draft preparation), and writing (review and editing); IW: writing (review and editing); SF: writing (review and editing).

Competing interests. The authors declare that they have no conflict of interest.

References

Aksenov, Y., Ivanov, V. V., Nurser, A. J. G., Bacon, S., Polyakov, I. V., Coward, A. C., Naveira-Garabato, A. C., and Beszczynska-Möller, A.: The Arctic Circumpolar Boundary Current, Journal of Geophysical Research, 116, C09 017, https://doi.org/10.1029/2010JC006637, 2011.

545 AMAP: AMAP Assessment 2018: Arctic Ocean Acidification., Arctic Monitoring and Assessment Programme (AMAP), Tromsø, Norway, ISBN 978-82-7971-107-0, 2018.

AMAP: AMAP Arctic Climate Change Update 2024: Key Trends and Impacts, Arctic Monitoring and Assessment Programme (AMAP), Tromsø, Norway, ISBN 978-82-7971-203-9, 2025.

ARCTIC_MULTIYEAR_PHY_002_003: ARCTIC_MULTIYEAR_PHY_002_003, https://doi.org/10.48670/moi-00007, 2024.

550 Bachman, S. D.: The GM+E Closure: A Framework for Coupling Backscatter with the Gent and McWilliams Parameterization, Ocean Modelling, 136, 85–106, https://doi.org/10.1016/j.ocemod.2019.02.006, 2019.

Barton, B. I., Lenn, Y.-D., and Lique, C.: Observed Atlantification of the Barents Sea Causes the Polar Front to Limit the Expansion of Winter Sea Ice, Journal of Physical Oceanography, 48, 1849–1866, https://doi.org/10.1175/JPO-D-18-0003.1, 2018.

Beszczynska-Möller, A., Fahrbach, E., Schauer, U., and Hansen, E.: Variability in Atlantic Water Temperature and Transport at the Entrance
555 to the Arctic Ocean, 1997-2010, ICES Journal of Marine Science, 69, 852–863, https://doi.org/10.1093/icesjms/fss056, 2012.

Bosse, A., Fer, I., Søiland, H., and Rossby, T.: Atlantic Water Transformation Along Its Poleward Pathway Across the Nordic Seas, Journal of Geophysical Research: Oceans, 123, 6428–6448, https://doi.org/10.1029/2018JC014147, 2018.

Copernicus Climate Change Service: ORAS5 Global Ocean Reanalysis Monthly Data from 1958 to Present, https://doi.org/10.24381/CDS.67E8EEB7, 2021.

560 Dai, A.: Dai and Trenberth Global River Flow and Continental Discharge Dataset, https://doi.org/10.5065/D6V69H1T, 2017.

Dmitrenko, I. A., Kirillov, S. A., Tremblay, L. B., Bauch, D., Hölemann, J. A., Krumpen, T., Kassens, H., Wegner, C., Heinemann, G., and Schröder, D.: Impact of the Arctic Ocean Atlantic Water Layer on Siberian Shelf Hydrography, Journal of Geophysical Research: Oceans, 115, https://doi.org/10.1029/2009JC006020, 2010.

Docquier, D., Grist, J. P., Roberts, M. J., Roberts, C. D., Semmler, T., Ponsoni, L., Massonnet, F., Sidorenko, D., Sein, D. V., Iovino, D.,
565 Bellucci, A., and Fichefet, T.: Impact of Model Resolution on Arctic Sea Ice and North Atlantic Ocean Heat Transport, Climate Dynamics, 53, 4989–5017, https://doi.org/10.1007/s00382-019-04840-y, 2019.

Dong, C., McWilliams, J. C., Liu, Y., and Chen, D.: Global Heat and Salt Transports by Eddy Movement, Nature Communications, 5, 3294, https://doi.org/10.1038/ncomms4294, 2014.

European Union-Copernicus Marine Service: Global Ocean Physics Reanalysis, https://doi.org/10.48670/MOI-00021, 2018.

570 Fox-Kemper, B., Adcroft, A., Böning, C. W., Chassignet, E. P., Curchitser, E., Danabasoglu, G., Eden, C., England, M. H., Gerdes, R., Greatbatch, R. J., Griffies, S. M., Hallberg, R. W., Hanert, E., Heimbach, P., Hewitt, H. T., Hill, C. N., Komuro, Y., Legg, S., Le Sommer, J., Masina, S., Marsland, S. J., Penny, S. G., Qiao, F., Ringler, T. D., Treguier, A. M., Tsujino, H., Uotila, P., and Yeager, S. G.: Challenges and Prospects in Ocean Circulation Models, Frontiers in Marine Science, 6, 65, https://doi.org/10.3389/fmars.2019.00065, 2019.

Gent, P. R. and McWilliams, J. C.: Isopycnal Mixing in Ocean Circulation Models, Journal of Physical Oceanography, 20, 150–155,
575 https://doi.org/10.1175/1520-0485(1990)020<0150:IMIOCM>2.0.CO;2, 1990.

Hallberg, R.: Using a Resolution Function to Regulate Parameterizations of Oceanic Mesoscale Eddy Effects, Ocean Modelling, 72, 92–103, https://doi.org/10.1016/j.ocemod.2013.08.007, 2013.

Heuzé, C., Zanowski, H., Karam, S., and Muilwijk, M.: The Deep Arctic Ocean and Fram Strait in CMIP6 Models, Journal of Climate, 36, 2551–2584, https://doi.org/10.1175/JCLI-D-22-0194.1, 2023.

580 Hewitt, H., Fox-Kemper, B., Pearson, B., Roberts, M., and Klocke, D.: The Small Scales of the Ocean May Hold the Key to Surprises, Nature Climate Change, 12, 496–499, https://doi.org/10.1038/s41558-022-01386-6, 2022.

Hirschi, J. J.-M., Barnier, B., Böning, C., Biastoch, A., Blaker, A. T., Coward, A., Danilov, S., Drijfhout, S., Getzlaff, K., Griffies, S. M., Hasumi, H., Hewitt, H., Iovino, D., Kawasaki, T., Kiss, A. E., Koldunov, N., Marzocchi, A., Mecking, J. V., Moat, B., Molines, J.-M., Myers, P. G., Penduff, T., Roberts, M., Treguier, A.-M., Sein, D. V., Sidorenko, D., Small, J., Spence, P., Thompson, L., Weijer, W., and

585 Xu, X.: The Atlantic Meridional Overturning Circulation in High-Resolution Models, Journal of Geophysical Research: Oceans, 125, e2019JC015 522, https://doi.org/10.1029/2019JC015522, 2020.

Holloway, G., Dupont, F., Golubeva, E., Häkkinen, S., Hunke, E., Jin, M., Karcher, M. J., Kauker, F., Maltrud, M., and Maqueda, M. A. M.: Water Properties and Circulation in Arctic Ocean Models, Journal of Geophysical Research, 112, C04S03, 2007.

Isachsen, P. E., Koszalka, I., and LaCasce, J. H.: Observed and Modeled Surface Eddy Heat Fluxes in the Eastern Nordic Seas, Journal of

590 Geophysical Research: Oceans, 117, https://doi.org/10.1029/2012JC007935, 2012.

Jakobsson, M., Mayer, L. A., Nilsson, J., Stranne, C., Calder, B., O'Regan, M., Farrell, J. W., Cronin, T. M., Brüchert, V., Chawarski, J., Eriksson, B., Fredriksson, J., Gemery, L., Glueder, A., Holmes, F. A., Jerram, K., Kirchner, N., Mix, A., Muchowski, J., Prakash, A., Reilly, B., Thornton, B., Ulfsbo, A., Weidner, E., Åkesson, H., Handl, T., Ståhl, E., Boze, L.-G., Reed, S., West, G., and Padman, J.: Ryder Glacier in Northwest Greenland Is Shielded from Warm Atlantic Water by a Bathymetric Sill, Communications Earth & Environment, 1,

595 1–10, https://doi.org/10.1038/s43247-020-00043-0, 2020.

Jansen, M. F., Adcroft, A., Khani, S., and Kong, H.: Toward an Energetically Consistent, Resolution Aware Parameterization of Ocean Mesoscale Eddies, Journal of Advances in Modeling Earth Systems, 11, 2844–2860, https://doi.org/10.1029/2019MS001750, 2019.

Karcher, M. J., Kauker, F., Gerdes, R., Hunke, E., and Zhang, J.: On the Dynamics of Atlantic Water Circulation in the Arctic Ocean, Journal of Geophysical Research, 112, C04S02, 2007.

600 Khosravi, N., Wang, Q., Koldunov, N., Hinrichs, C., Semmler, T., Danilov, S., and Jung, T.: The Arctic Ocean in CMIP6 Models: Biases and Projected Changes in Temperature and Salinity, Earth's Future, 10, e2021EF002 282, https://doi.org/10.1029/2021EF002282, 2022.

Kusters, N., Balwada, D., and Groeskamp, S.: Global Observational Estimates of Mesoscale Eddy Driven Quasi-Stokes Velocity and Buoyancy Diffusivity - Data, https://doi.org/10.1029/2025GL115802, 2025.

Li, S., Lin, P., Dou, T., Xiao, C., Itoh, M., Kikuchi, T., and Qin, D.: Upwelling of Atlantic Water in Barrow Canyon, Chukchi Sea, Journal of

605 Geophysical Research: Oceans, 127, e2021JC017 839, https://doi.org/10.1029/2021JC017839, 2022.

Li, X., Wang, Q., Danilov, S., Koldunov, N., Liu, C., Müller, V., Sidorenko, D., and Jung, T.: Eddy Activity in the Arctic Ocean Projected to Surge in a Warming World, Nature Climate Change, 14, 156–162, https://doi.org/10.1038/s41558-023-01908-w, 2024.

Lind, S., Ingvaldsen, R. B., and Furevik, T.: Arctic Warming Hotspot in the Northern Barents Sea Linked to Declining Sea-Ice Import, Nature Climate Change, 8, 634–639, https://doi.org/10.1038/s41558-018-0205-y, 2018.

610 Loose, N., Bachman, S., Grooms, I., and Jansen, M.: Diagnosing Scale-Dependent Energy Cycles in a High-Resolution Isopycnal Ocean Model, Journal of Physical Oceanography, 53, https://doi.org/10.1175/JPO-D-22-0083.1, 2022.

Mak, J., Maddison, J. R., Marshall, D. P., and Munday, D. R.: Implementation of a Geometrically Informed and Energetically Constrained Mesoscale Eddy Parameterization in an Ocean Circulation Model, Journal of Physical Oceanography, 48, 2363–2382, https://doi.org/10.1175/JPO-D-18-0017.1, 2018.

615   Mak, J., Maddison, J. R., Marshall, D. P., Ruan, X., Wang, Y., and Yeow, L.: Scale-Awareness in an Eddy Energy Constrained Mesoscale
Eddy Parameterization, Journal of Advances in Modeling Earth Systems, 15, e2023MS003 886, https://doi.org/10.1029/2023MS003886,
2023.

Marnela, M., Rudels, B., Houssais, M.-N., Beszczynska-Möller, A., and Eriksson, P. B.: Recirculation in the Fram Strait and Transports of
Water in and North of the Fram Strait Derived from CTD Data, Ocean Science, 9, 499–519, https://doi.org/10.5194/os-9-499-2013, 2013.

620   Meneghello, G., Marshall, J., Lique, C., Isachsen, P. E., Doddridge, E., Campin, J.-M., Regan, H., and Talandier, C.: Genesis and Decay
of Mesoscale Baroclinic Eddies in the Seasonally Ice-Covered Interior Arctic Ocean, Journal of Physical Oceanography, 51, 115–129,
https://doi.org/10.1175/JPO-D-20-0054.1, 2021.

Muilwijk, M., Smedsrud, L. H., Ilicak, M., and Drange, H.: Atlantic Water Heat Transport Variability in the 20th Century
Arctic Ocean From a Global Ocean Model and Observations, Journal of Geophysical Research: Oceans, 123, 8159–8179,
625   https://doi.org/10.1029/2018JC014327, 2018.

Muilwijk, M., Ilicak, M., Cornish, S. B., Danilov, S., Gelderloos, R., Gerdes, R., Haid, V., Haine, T. W. N., Johnson, H. L., Kostov,
Y., Kovács, T., Lique, C., Marson, J. M., Myers, P. G., Scott, J., Smedsrud, L. H., Talandier, C., and Wang, Q.: Arctic Ocean Re-
sponse to Greenland Sea Wind Anomalies in a Suite of Model Simulations, Journal of Geophysical Research: Oceans, 124, 6286–6322,
https://doi.org/10.1029/2019JC015101, 2019.

630   Nøst, O. A. and Isachsen, P. E.: The Large-Scale Time-Mean Ocean Circulation in the Nordic Seas and Arctic Ocean Estimated from
Simplified Dynamics, Journal Of Marine Research, 61, 175–210, 2003.

Østerhus, S., Woodgate, R. A., Valdimarsson, H., Turrell, B., de Steur, L., Quadfasel, D., Olsen, S. M., Moritz, M., Lee, C. M., Larsen,
K. M. H., Jónsson, S., Johnson, C., Jochumsen, K., Hansen, B., Curry, B., Cunningham, S., and Berx, B.: Arctic Mediterranean Ex-
changes: A Consistent Volume Budget and Trends in Transports from Two Decades of Observations, Ocean Science, 15, 379–399,
635   https://doi.org/10.5194/os-15-379-2019-supplement, 2019.

Pnyushkov, A., Polyakov, I. V., Padman, L., and Nguyen, A. T.: Structure and Dynamics of Mesoscale Eddies over the Laptev Sea Continental
Slope in the Arctic Ocean, Ocean Science, 14, 1329–1347, https://doi.org/10.5194/os-14-1329-2018, 2018.

Polyakov, I. V., Rippeth, T. P., Fer, I., Alkire, M. B., Baumann, T. M., Carmack, E. C., Ingvaldsen, R., Ivanov, V. V., Janout, M., Lind, S.,
Padman, L., Pnyushkov, A. V., and Rember, R.: Weakening of Cold Halocline Layer Exposes Sea Ice to Oceanic Heat in the Eastern Arctic
640   Ocean, Journal of Climate, 33, 8107–8123, https://doi.org/10.1175/JCLI-D-19-0976.1, 2020.

Polyakov, I. V., Ingvaldsen, R. B., Pnyushkov, A. V., Bhatt, U. S., Francis, J. A., Janout, M., Kwok, R., and Skagseth, Ø.: Fluctuating Atlantic
Inflows Modulate Arctic Atlantification, Science, 381, 972–979, https://doi.org/10.1126/science.adh5158, 2023.

Rantanen, M., Karpechko, A. Y., Lipponen, A., Nordling, K., Hyvärinen, O., Ruosteenoja, K., Vihma, T., and Laaksonen, A.: The
Arctic Has Warmed Nearly Four Times Faster than the Globe since 1979, Communications Earth & Environment, 3, 1–10,
645   https://doi.org/10.1038/s43247-022-00498-3, 2022.

Redi, M. H.: Oceanic Isopycnal Mixing by Coordinate Rotation, Journal of Physical Oceanography, 12, 1154–1158,
https://doi.org/10.1175/1520-0485(1982)012<1154:OIMBCR>2.0.CO;2, 1982.

Ruan, X., Couespel, D., Lévy, M., Li, J., Mak, J., and Wang, Y.: Combined Physical and Biogeochemical Assessment of Mesoscale
Eddy Parameterisations in Ocean Models: Eddy-induced Advection at Eddy-Permitting Resolutions, Ocean Modelling, 190, 102 396,
650   https://doi.org/10.1016/j.ocemod.2024.102396, 2024.

Rudels, B. and Carmack, E.: Arctic Ocean Water Mass Structure and Circulation, Oceanography, 35, 52–65,
https://doi.org/10.5670/oceanog.2022.116, 2022.

Rudels, B., Anderson, L. G., Eriksson, P., Fahrbach, E., Jakobsson, M., Jones, E. P., Melling, H., Prinsenberg, S., Schauer, U., and Yao, T.: Observations in the Ocean, in: The ACSYS Decade and Beyond, Atmospheric and Oceanographic Sciences Library 43, edited by Lemke,

655   P. and Jacobi, H., pp. 117–198, Springer Netherlands, Dordrecht, https://doi.org/10.1007/978-94-007-2027-5_4, 2011.

Rudels, B., Korhonen, M., Schauer, U., Pisarev, S., Rabe, B., and Wisotzki, A.: Circulation and Transformation of Atlantic Water in the Eurasian Basin and the Contribution of the Fram Strait Inflow Branch to the Arctic Ocean Heat Budget, Progress in Oceanography, 132, 128–152, https://doi.org/10.1016/j.pocean.2014.04.003, 2015.

Schauer, U. and Beszczynska-Möller, A.: Problems with Estimation and Interpretation of Oceanic Heat Transport – Conceptual Remarks for

660   the Case of Fram Strait in the Arctic Ocean, Ocean Science, 5, 487–494, https://doi.org/10.5194/os-5-487-2009, 2009.

Schauer, U., Beszczynska-Möller, A., Walczowski, W., Fahrbach, E., Piechura, J., and Hansen, E.: Variation of Measured Heat Flow through the Fram Strait between 1997 and 2006, in: Arctic–Subarctic Ocean Fluxes, pp. 65–85, Springer, 2008.

Shu, Q., Wang, Q., Su, J., Li, X., and Qiao, F.: Assessment of the Atlantic Water Layer in the Arctic Ocean in CMIP5 Climate Models, Climate Dynamics, 53, 5279–5291, https://doi.org/10.1007/s00382-019-04870-6, 2019.

665   Shu, Q., Wang, Q., Guo, C., Song, Z., Wang, S., He, Y., and Qiao, F.: Arctic Ocean Simulations in the CMIP6 Ocean Model Intercomparison Project (OMIP), Geoscientific Model Development, 16, 2539–2563, https://doi.org/10.5194/gmd-16-2539-2023, 2023.

Smedsrud, L. H., Ingvaldsen, R., Nilsen, J. E. Ø., and Skagseth, O.: Heat in the Barents Sea: Transport, Storage, and Surface Fluxes, Ocean Science, 6, 219–234, https://doi.org/10.5194/os-6-219-2010, 2010.

Smedsrud, L. H., Muilwijk, M., Brakstad, A., Madonna, E., Lauvset, S. K., Spensberger, C., Born, A., Eldevik, T., Drange, H., Jeansson, E.,

670   Li, C., Olsen, A., Skagseth, Ø., Slater, D. A., Straneo, F., Våge, K., and Årthun, M.: Nordic Seas Heat Loss, Atlantic Inflow, and Arctic Sea Ice Cover Over the Last Century, Reviews of Geophysics, 60, e2020RG000 725, https://doi.org/10.1029/2020RG000725, 2022.

Steele, M., Morley, R., and Ermold, W.: PHC: A Global Ocean Hydrography with a High-Quality Arctic Ocean, Journal of Climate, 14, 2079–2087, https://doi.org/10.1175/1520-0442(2001)014<2079:PAGOHW>2.0.CO;2, 2001.

Strehl, A.-M., Våge, K., Smedsrud, L. H., and Barreyre, T.: A 70-Year Perspective on Water-Mass Transformation in the Greenland Sea:

675   From Thermobaric to Thermal Convection, Progress in Oceanography, 227, 103 304, https://doi.org/10.1016/j.pocean.2024.103304, 2024.

Stroeve, J. and Notz, D.: Changing State of Arctic Sea Ice across All Seasons, Environmental Research Letters, 13, 103 001, https://doi.org/10.1088/1748-9326/aade56, 2018.

Timmermans, ML. and Marshall, J.: Understanding Arctic Ocean Circulation: A Review of Ocean Dynamics in a Changing Climate, Journal of Geophysical Research, 125, C04S02, https://doi.org/10.1029/2018JC014037, 2020.

680   Treguier, A. M., Held, I. M., and Larichev, V. D.: Parameterization of Quasigeostrophic Eddies in Primitive Equation Ocean Models, Journal of Physical Oceanography, 27, 567–580, https://doi.org/10.1175/1520-0485(1997)027<0567:POQEIP>2.0.CO;2, 1997.

Tsubouchi, T., Bacon, S., Naveira Garabato, A. C., Aksenov, Y., Laxon, S. W., Fahrbach, E., Beszczynska-Möller, A., Hansen, E., Lee, C. M., and Ingvaldsen, R. B.: The Arctic Ocean in Summer: A Quasi-Synoptic Inverse Estimate of Boundary Fluxes and Water Mass Transformation, Journal of Geophysical Research, 117, C01 024, https://doi.org/10.1029/2011JC007174, 2012.

685   Tsubouchi, T., Våge, K., Hansen, B., Larsen, K. M. H., Østerhus, S., Johnson, C., Jónsson, S., and Valdimarsson, H.: Increased Ocean Heat Transport into the Arctic Mediterranean over the Period 1993-2016, 2020.

Tsujino, H., Urakawa, S., Nakano, H., Small, R. J., Kim, W. M., Yeager, S. G., Danabasoglu, G., Suzuki, T., Bamber, J. L., Bentsen, M., Böning, C. W., Bozec, A., Chassignet, E. P., Curchitser, E., Boeira Dias, F., Durack, P. J., Griffies, S. M., Harada, Y., Ilicak, M., Josey, S. A., Kobayashi, C., Kobayashi, S., Komuro, Y., Large, W. G., Le Sommer, J., Marsland, S. J., Masina, S., Scheinert, M., Tomita, H.,

690   Valdivieso, M., and Yamazaki, D.: JRA-55 Based Surface Dataset for Driving Ocean–Sea-Ice Models (JRA55-do), Ocean Modelling, 130, 79–139, https://doi.org/10.1016/j.ocemod.2018.07.002, 2018.

von Appen, W.-J., Baumann, T., Janout, M. A., Koldunov, N., Lenn, Y.-D., Pickart, R., Scott, R., and Wang, Q.: Eddy Kinetic Energy in the Arctic Ocean from Moored Velocity Observations, https://doi.org/10.1594/PANGAEA.941165, 2022.

von Appen, W.-J., Baumann, T. M., Janout, M., Koldunov, N., and Lenn, Y.-D.: Eddies and the Distribution of Eddy Kinetic Energy in the
695   Arctic Ocean, Oceanography, 35, 42–51, https://doi.org/10.5670/oceanog.2022.122, 2022.

Wang, Q., Shu, Q., Bozec, A., Chassignet, E. P., Fogli, P. G., Fox-Kemper, B., Hogg, A. M., Iovino, D., Kiss, A. E., Koldunov, N., Le Sommer, J., Li, Y., Lin, P., Liu, H., Polyakov, I., Scholz, P., Sidorenko, D., Wang, S., and Xu, X.: Impact of Increased Resolution on Arctic Ocean Simulations in Ocean Model Intercomparison Project Phase 2 (OMIP-2), Geoscientific Model Development, 17, 347–379, https://doi.org/10.5194/gmd-17-347-2024, 2024.

700   Wefing, A.-M., Casacuberta, N., Christl, M., Gruber, N., and Smith, J. N.: Circulation Timescales of Atlantic Water in the Arctic Ocean Determined from Anthropogenic Radionuclides, Ocean Science, 17, 111–129, https://doi.org/10.5194/os-17-111-2021, 2021.

Wekerle, C., Wang, Q., Danilov, S., Schourup-Kristensen, V., von Appen, W.-J., and Jung, T.: Atlantic Water in the Nordic Seas: Locally Eddy-Permitting Ocean Simulation in a Global Setup, Journal of Geophysical Research: Oceans, 122, 914–940, https://doi.org/10.1002/2016JC012121, 2017.

705   Wekerle, C., McPherson, R., von Appen, W.-J., Wang, Q., Timmermann, R., Scholz, P., Danilov, S., Shu, Q., and Kanzow, T.: Atlantic Water Warming Increases Melt below Northeast Greenland's Last Floating Ice Tongue, Nature Communications, 15, 1336, https://doi.org/10.1038/s41467-024-45650-z, 2024.

Zhang, J. and Steele, M.: Effect of Vertical Mixing on the Atlantic Water Layer Circulation in the Arctic Ocean, Journal of Geophysical Research, 112, C04S04, https://doi.org/10.1029/2006JC003732, 2007.

Appendix A: Snapshots of relative vorticity and potential temperature

To provide further evidence of the eddy dampening effect of the GM scheme we show daily snapshots of relative vorticity and potential temperature. In Figure A1 it is seen that the high resolution experiment (ARCTIC12) has a much higher relative vorticity and a more vigorous eddy field in both the Nordic Seas and Arctic Ocean, especially close to the boundary currents along the continental slopes. In Figure A2 it is seen how warm eddy like structures detach from the boundary current in ARCTIC12. In the intermediate resolutions ARCTIC-noGM has higher relative vorticity, and more warm water eddy structures shedding of the boundary current than the experiments with eddy-induced transport, showing the dampening impact on the eddy field by the GM scheme.
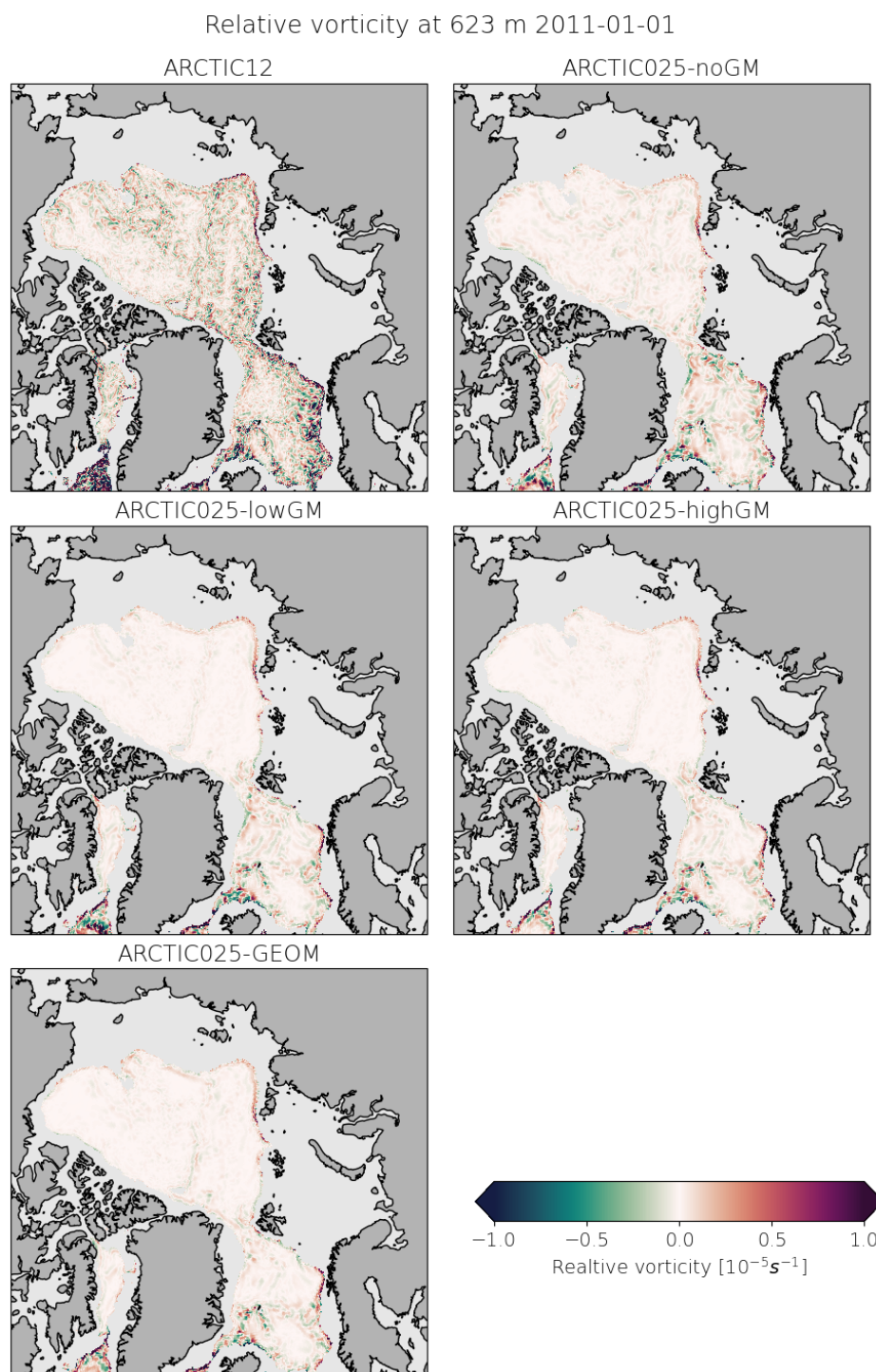
Figure A1. Daily snapshot (1st of January 2011) of relative vorticity in the AW layer (623 m depth) computed for the different experiments.
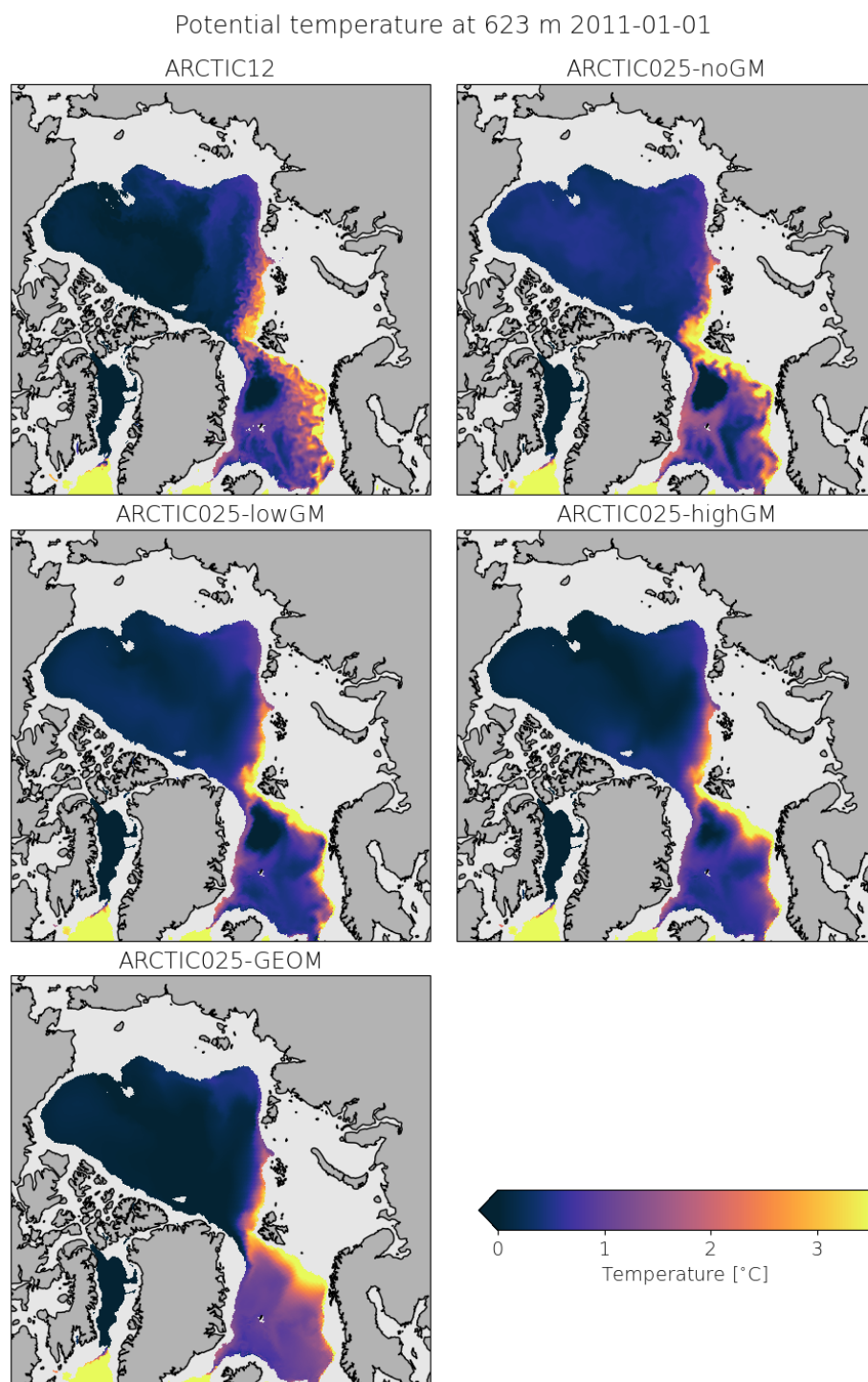
Figure A2. Daily snapshot (1st of January 2011) of potential temperature in the AW layer (623 m depth) computed for the different experiments.